



AFRL-OSR-VA-TR-2014-0283

---

**DEVELOPMENT AND APPLICATION OF ACOUSTIC MATERIALS WITH LOCALLY RESONANT MICROSTR**

**Chin Teh Sun  
PURDUE UNIVERSITY**

---

**10/21/2014  
Final Report**

**DISTRIBUTION A: Distribution approved for public release.**

**Air Force Research Laboratory  
AF Office Of Scientific Research (AFOSR)/ RTD  
Arlington, Virginia 22203  
Air Force Materiel Command**

<b>REPORT DOCUMENTATION PAGE</b>				<b>Form Approved OMB No. 0704-0188</b>	
<small>Public reporting burden for this collection of information is estimated to average 1 hour per response, including the time for reviewing instructions, searching data sources, gathering and maintaining the data needed, and completing and reviewing the collection of information. Send comments regarding this burden estimate or any other aspect of this collection of information, including suggestions for reducing this burden to Washington Headquarters Service, Directorate for Information Operations and Reports, 1215 Jefferson Davis Highway, Suite 1204, Arlington, VA 22202-4302, and to the Office of Management and Budget, Paperwork Reduction Project (0704-0188) Washington, DC 20503.</small>					
<b>PLEASE DO NOT RETURN YOUR FORM TO THE ABOVE ADDRESS.</b>					
<b>1. REPORT DATE</b> (DD-MM-YYYY) 10/15/2014		<b>2. REPORT TYPE</b> Final Report		<b>3. DATES COVERED</b> (From - To) 04/15/2010-04/14/2014	
<b>4. TITLE AND SUBTITLE</b> Development and Application of Acoustic Metamaterials with Locally Resonant Microstructures				<b>5a. CONTRACT NUMBER</b> 	
				<b>5b. GRANT NUMBER</b> FA9550-10-1-0061	
				<b>5c. PROGRAM ELEMENT NUMBER</b> 61102F	
<b>6. AUTHOR(S)</b> Chin Teh Sun				<b>5d. PROJECT NUMBER</b> 	
				<b>5e. TASK NUMBER</b> 	
				<b>5f. WORK UNIT NUMBER</b> 	
<b>7. PERFORMING ORGANIZATION NAME(S) AND ADDRESS(ES)</b> Purdue University				<b>8. PERFORMING ORGANIZATION REPORT NUMBER</b> 	
<b>9. SPONSORING/MONITORING AGENCY NAME(S) AND ADDRESS(ES)</b> Air Force Office of Scientific Research (AFOSR), 875 N. Randolph Street, Arlington, VA 22203				<b>10. SPONSOR/MONITOR'S ACRONYM(S)</b> Program Manager: Dr. B. L. Lee	
				<b>11. SPONSORING/MONITORING AGENCY REPORT NUMBER</b> 	
<b>12. DISTRIBUTION AVAILABILITY STATEMENT</b> Approved for Public Release					
<b>13. SUPPLEMENTARY NOTES</b> 					
<b>14. ABSTRACT</b> 					
<b>15. SUBJECT TERMS</b> 					
<b>16. SECURITY CLASSIFICATION OF:</b>			<b>17. LIMITATION OF ABSTRACT</b>	<b>18. NUMBER OF PAGES</b>	<b>19a. NAME OF RESPONSIBLE PERSON</b>
a. REPORT	b. ABSTRACT	c. THIS PAGE			<b>19b. TELEPHONE NUMBER</b> (Include area code)

## **Final Report**

# **Development and Application of Acoustic Metamaterials with Locally Resonant Microstructures**

**Prepared by**

**C.T. Sun  
School of Aeronautics and Astronautics  
Purdue University  
West Lafayette, IN 47907**

**Submitted to  
Air Force Office of Scientific Research,  
875 N. Randolph Street, AFOSR/NA, Suite 325  
Arlington, VA 22203**

**October 15, 2014**

## 1. INTRODUCTION

A metamaterial is a material that gains its properties from its structure rather than from its constituent material phases. Metamaterials with negative refractive index is one of the most active topics among the research community. The idea of it traces back to 1968 when Veselago (1968) postulated a theory for possible materials having negative electric permittivity ( $\epsilon$ ) and magnetic permeability ( $\mu$ ), and hence resulting in a negative refractive index. Three decades later, Smith et al. (2000) proposed a design of making an artificial material that exhibits a frequency region in the microwave regime with simultaneously negative permittivity and negative permeability. They demonstrated both by numerical simulation and experiment the unusual physical phenomena. In the same year, Pendry (2000) proposed a practical application of this type of electromagnetic metamaterials: a perfect lens, capable of imaging objects and fine structures that are much smaller than the wavelength of light. As a result of this development of novel electromagnetic metamaterials, researchers extended the same concept to the acoustic counterparts immediately. For the negative-index acoustic metamaterials, basically it is to find materials possessing negative mass density and negative modulus because these two material properties govern the wave motions in acoustic (or elastic) materials. However, in contrast to the natural negative electric permittivity, no natural material has been found to possess negative mass density or negative modulus. This difficulty brings about some barriers to the realization of acoustic counterparts.

Some recent developments have theoretically shown that acoustic/elastic metamaterials could be realized. Liu et al. (2000) investigated a new type of composite fabricated using lead balls coated with silicon rubber in the epoxy matrix. Around the local resonance frequencies, the composite behaves as a material with effective negativity. Such an anomalous response of the system is the consequence of the coupling of the long-wavelength elastic wave in the host medium with the localized vibration motion of the spheres. Recently, Milton and Willis (2007) and Huang et al. (2009) have presented a theoretical foundation for the concept of negative effective mass.

The field of metamaterials is still in its infancy. Further studies are needed to fully understand the complex behavior of these materials. More designs of microstructures are desired to produce new metamaterials with new properties and some of the unusual behavior of metamaterials predicted by theoretical models need to be verified experimentally. More importantly, practical applications of metamaterials should be explored.

## 2. OBJECTIVE

The purpose of this research is to design, fabricate, and study new acoustic metamaterials with a negative effective mass density and modulus. Through this study, it is anticipated that the implications to material and structural applications of the negative effective mass and modulus of metamaterials can be fully understood. Moreover, more microstructures for metamaterials will be designed and studied. The 3D printing technology will be utilized to produce these complicated microstructures and metamaterial specimens for experiments.

### 3. APPROACH

The key feature of a metamaterial that may exhibit a negative effective mass density and modulus takes the form of a continuum containing local resonators. This configuration yields a local resonance frequency, a feature essential to the desired metamaterial. In view of this, we focus the effort on the design of new resonator microstructures, perform modeling and simulations of the dynamic behavior of these materials, conduct experiments to verify the model predictions, and identify applications of these metamaterials.

## 4. Acoustic Metamaterial with Extreme Young's Moduli

### 4.1 Introduction

The subject of metamaterials has recently attracted much attention of researchers. Generally speaking, metamaterials are considered a new class of composites with man-made subwavelength microstructures that exhibit unusual behavior not readily observed in natural materials. Veselago (1968) first postulated a theory for possible materials having negative electric permittivity and magnetic permeability, and hence resulting in a backward wave and a negative refractive index. This concept, however, did not stimulate much interest among researchers at that time. Three decades later, Smith et al. (2000) investigated the possibility of making left-handed electromagnetic metamaterials. Pendry (2000) proposed a perfect lens made of left-handed metamaterial that would lead to practical applications. Shelby et al. (2001) demonstrated the experimental verification of a negative index of refraction. Since then, numerous works regarding metamaterials have been engaged and great numbers of publications are poured in.

Motivated by the mathematical analogy between acoustic and electromagnetic waves, researchers have attempted to find the counterpart left-handed acoustic metamaterials, namely, materials having negative mass density and negative elastic modulus simultaneously. Nevertheless, in contrast to the natural negative electric permittivity, no natural material has been found to possess either negative mass density or negative modulus. This makes the realization of acoustic counterpart metamaterials more difficult. To this end, some researchers have resorted to man-made microstructures to achieve an apparent effect of negative mass density (Liu et al., 2005; Milton and Willis, 2007; Yao et al., 2008; Huang et al., 2009; Huang and Sun, 2009; Lee et al., 2009a). Most of these researchers employed mechanical resonators as “microstructures” to form the acoustic metamaterial, which was first introduced by Liu et al. (2000). It was found that if the acoustic metamaterial is treated as a classical elastic solid, then its effective mass density would be frequency-dependent and become negative in certain frequency range. Recently, acoustic metamaterials, possessing negative effective modulus, were proposed and studied (Fang et al., 2006; Lee et al., 2009b). These “metamaterials” are, however, structures having the form of a pipe with lateral Helmholtz resonators or side holes designed to manipulate acoustic waves. Attenuation of waves was also confirmed experimentally within the negative range of effective modulus.

It is also of interest to note a type of composite materials with negative-stiffness inclusions proposed by Lakes et al. (2001) in which the working mechanism of this type of materials is fundamentally different than that of the aforementioned metamaterials. In Lakes' case, negative stiffness can occur, for instance, when the deforming object has stored energy. This property is usually unstable but has been shown theoretically that negative stiffness can be stabilized within a positive-stiffness matrix (Drugan, 2007). They (Lakes et al., 2001; Drugan, 2007) found that the resulting composites exhibit extreme mechanical damping and large anomalies in stiffness, as a consequence of the high local strains that result from the inclusions which deform more than the composite as a whole. Jaglinski et al. (2007) further showed that this kind of composite materials exhibit a viscoelastic modulus substantially greater than that of diamond.

In the present paper we focus on the acoustic metamaterials of the local-resonance kind. First, a model that exhibits negative effective Young's modulus is proposed and its dynamic characteristics are investigated. The wave propagation behavior of the one-dimensional system is subsequently studied. Some numerical simulations on wave attenuation and filtering in the acoustic metamaterials are presented at the end.

## 4.2. A mechanical model with extreme and negative effective Young's modulus

### 4.2.1 A unit model and its effective Young's modulus

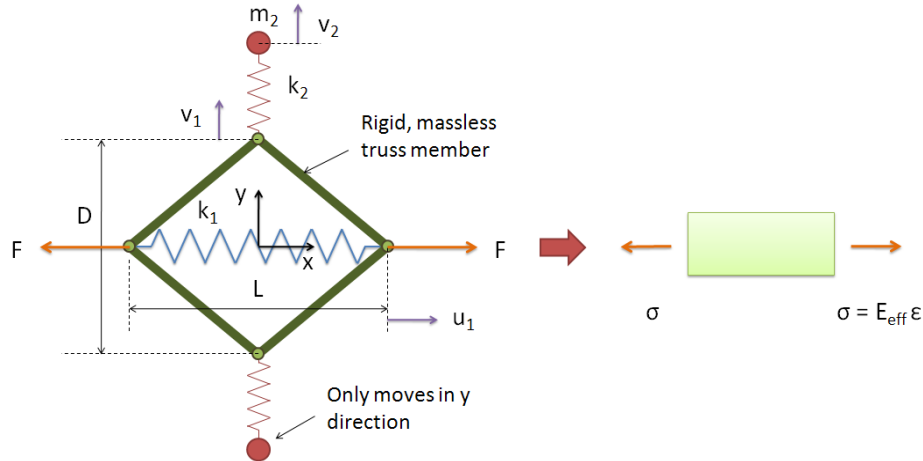


Figure 4.1 A unit of the mechanical model and the effective continuum

Consider a mechanical model shown in Figure 4.11 representing a unit of a 1D acoustic metamaterial. A spring with elastic constant  $k_1$  and length  $L$  in its equilibrium state is connected to four rigid and massless truss members. The main body is assembled symmetrically as shown to support two sets of microstructures consisting of springs with elastic constant  $k_2$  and masses  $m_2$ . Point mass  $m_2$  is allowed to move only in  $y$  direction.

Consider a dynamic test of stress-strain relation by applying a symmetrical pair of harmonic forces  $F$  in the  $x$  direction as shown in Figure 4.1. The equations of motion of the system are readily obtained as

$$F = 2k_1u_1 + \frac{L}{D}k_2(v_2 - v_1) \quad (4.1)$$

$$m_2 \frac{\partial^2 v_2}{\partial t^2} = k_2(v_1 - v_2) \quad (4.2)$$

In the equations above, the external force assumes harmonic complex form  $F = \hat{F}e^{i\omega t}$ , where  $\hat{F}$  is the excitation force and  $\omega$  is the excitation frequency. Assuming small displacements, we have

$$v_1 = -\frac{(L-u_1)u_1}{D} + \frac{(L-u_1)^2 u_1^2}{D^3} + \dots \approx -\frac{L}{D}u_1 \quad (4.3)$$

The force-displacement relation is obtained by letting the displacement fields be  $u_1 = \hat{u}_1 e^{i\omega t}$  and  $v_2 = \hat{v}_2 e^{i\omega t}$  and substituting the harmonic displacements in equations (4.1) and (4.2). We obtain

$$\hat{F} = 2 \left\{ k_1 + \frac{1}{2} \frac{k_2 \omega^2}{\omega^2 - \omega_0^2} \left( \frac{L}{D} \right)^2 \right\} \hat{u}_1 \quad (4.4)$$

If the mechanical system is to be represented by a 1D elastic solid as shown in Figure 1, the stress-strain relation of the effective continuum is

$$\hat{\sigma} = E_{eff} \hat{\epsilon} \quad (4.5)$$

$\hat{\sigma} = \hat{F}/A$  ( $A$  is the cross-section of the elastic solid) and  $\hat{\epsilon} = \hat{u}/L$  are average stress and strain, respectively, of the continuum element, and  $E_{eff}$  is the effective Young's modulus of the 1D elastic solid. Since the models in the present study are 1D, in the following the term “modulus” is referred to “Young's modulus” unless specified otherwise. To make the two models dynamically equivalent, equations (4.4) and (4.5) must be the same and, thus, the effective modulus of the elastic solid would take the form

$$\frac{E_{eff}}{E_0} = 1 + \frac{\delta \mu}{2} \frac{\eta^2}{\eta^2 - 1} \quad (4.6)$$

where  $E_0 = k_1 L/A$  is the static Young's modulus,  $\eta = \omega/\omega_0$  is non-dimensional wave frequency in which  $\omega_0 = \sqrt{k_2/m_2}$ ,  $\delta = k_2/k_1$ , and  $\mu = (L/D)^2$ .

## 2.2 Discussion

From equation (4.6), we note that the effective modulus is frequency-dependent and is unbounded when the driving frequency  $\omega$  is equal to the local resonance frequency,

i.e.,  $\eta = 1$ . The dynamic stress-strain curves illustrating the effective moduli corresponding to different frequencies are schematically plotted in Figure 4.2. In the figure, the frequency-dependent effective modulus is seen to approach infinity when  $\omega \rightarrow \omega_0 = \sqrt{k_2/m_2}$ , and approaches zero when  $\omega \rightarrow \omega^*$  with

$$\omega^* = \omega_0 \sqrt{2/(2 + \delta\mu)} \quad (4.7)$$

For frequencies in between  $\omega_0$  and  $\omega^*$ , the effective modulus becomes negative.

Figure 3 shows an example of the non-dimensionalized effective modulus and the displacement ratio  $v_2/u_1$  with respect to excitation frequency. In the example, the material and geometrical constants are selected as:  $\delta = k_2/k_1 = 2$ ,  $\mu = (L/D)^2 = 1$ . For harmonic vibrations, the displacement ratio  $v_2/u_1$  is obtained from equation (4.2) as

$$\frac{v_2}{u_1} = \frac{\sqrt{\mu}}{\eta^2 - 1} \quad (4.8)$$

It is clearly seen that for frequencies between  $\omega_0$  and  $\omega^*$ , the effective modulus and the ratio  $v_2/u_1$  would become negative.

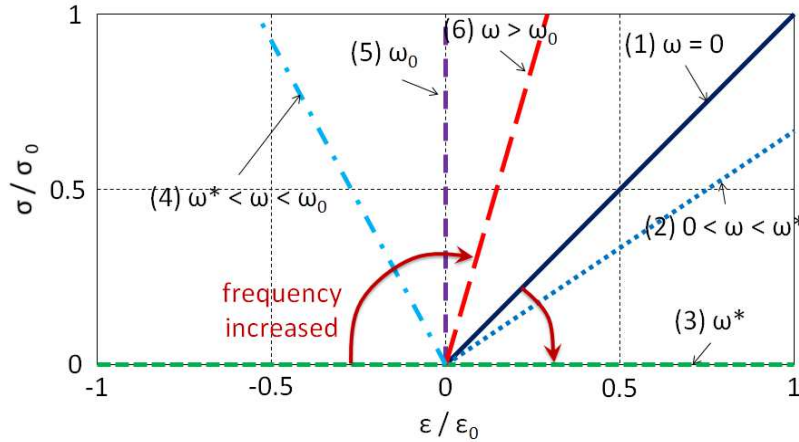


Figure 4.2 Stress-strain curves for various frequencies.  $\sigma_0$ ,  $\varepsilon_0$ , and  $E_0$  are values for the corresponding static case



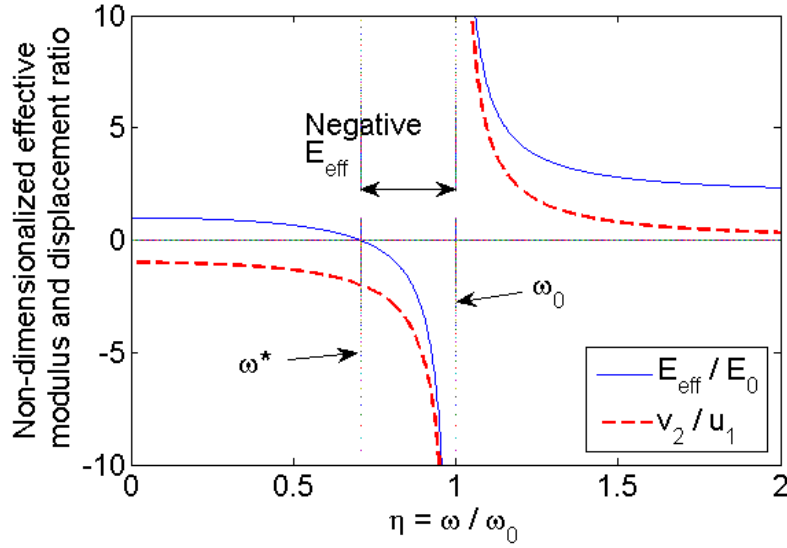


Figure 4.3 Dynamic behavior of the model with respect to excitation frequency

### 4.3 Significance of negative effective Young's modulus

#### 4.3.1 1D lattice model

Consider a 1D model consisting of a large number of resonator units as shown in Figure 4.4. The mass of the background material in this 1D model is lumped to nodes of the lattice system and denoted by  $m_1$ . The equations of motion for the  $j^{\text{th}}$  unit are

$$m_1 \frac{\partial^2 u_1^{(j)}}{\partial t^2} = k_1(u_1^{(j-1)} - u_1^{(j)}) + k_1(u_1^{(j+1)} - u_1^{(j)}) - 2k_2(v_2^{(j-1)} - v_1^{(j-1)}) \frac{L}{2D} + 2k_2(v_2^{(j)} - v_1^{(j)}) \frac{L}{2D} \quad (4.9)$$

$$m_2 \frac{\partial^2 v_2^{(j)}}{\partial t^2} = k_2(v_1^{(j)} - v_2^{(j)}) \quad (4.10)$$

In deriving equations (4.9- 4.10), the geometrical relationship,  $v_1^{(j)} = -\frac{L}{2D}(u_1^{(j+1)} - u_1^{(j)})$ , is used. For the harmonic wave motion given by  $u_1^{(j+n)} = \hat{u}_1 e^{i(\xi X^* + n\xi - \eta T^*)}$  and  $v_2^{(j+n)} = \hat{v}_2 e^{i(\xi X^* + n\xi - \eta T^*)}$ , we derive the dispersion relation from the equations of motion with the result:

$$H(\eta, \xi) = \eta^4 - \left\{ 1 + 2\left(\frac{\theta}{\delta} + \frac{\theta\mu}{2}\right)(1 - \cos \xi) \right\} \eta^2 + 2\frac{\theta}{\delta}(1 - \cos \xi) = 0 \quad (4.11)$$

where  $\theta = m_2 / m_1$ ,  $\xi = qL$  is non-dimensional wave number,  $X^* = x/L$  is non-dimensional distance, and  $T^* = \omega_0 t$  is non-dimensional time. The dispersion curves are plotted in Figures 4.5 and 4.6, respectively, for two cases:

Case 1:  $\theta = 2$ ,  $\delta = 0.5$ ,  $\mu = 4$ .

Case 2:  $\theta = 0.5$ ,  $\delta = 5$ ,  $\mu = 1$ .

In either case, a band gap associated with the local resonance is present. Unlike the mass-in-mass lattice system studied by Huang et al. (2009), the local resonance frequency of the present system is located at the upper bound of the band gap. For frequencies in the band gap, the wave number must assume a complex form  $\xi = \alpha + i\beta$  in order to satisfy the dispersion equation (4.11). This implies that waves with a frequency in the band gap would attenuate spatially. It is noted that, in the present case, the maximum attenuation factor  $\beta$ , does not occur at the local resonance frequency.

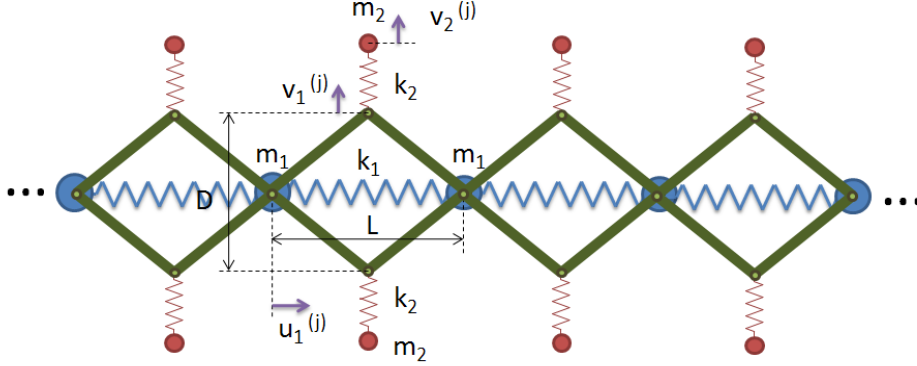


Figure 4.4 A 1D lattice model

It is of interest to represent the 1D lattice system by a 1D elastic solid with an effective Young's modulus  $E_{eff}$ . Since the dispersion curves depict the dynamic behavior of the 1D lattice system, the representative elastic solid should match the dispersion behavior. First, take the effective mass of the system to be the average mass of the unit, namely,  $\rho_{eff} = \rho_0 = m_1 / (AL)$ . From the classical wave equation of an elastic solid, the dispersion relation is given by  $\rho_0 \omega^2 = E_{eff} q^2$ . Next, substitute this dispersion relation in equation (4.11) to obtain

$$\frac{E_{eff}}{E_0} = \frac{\delta}{\theta} \eta^2 \left\{ \cos^{-1} \left[ 1 - \frac{(\eta^2 - 1)\eta^2}{2[(\theta/\delta + \theta\mu/2)\eta^2 - \theta/\delta]} \right] \right\}^{-2} \quad (4.12)$$

Alternatively, we can adopt the effective modulus given by equation (4.6) which is obtained from the unit (see Figure 4.1) by a dynamic stiffness equivalence method. Effective moduli given by equations (4.6) and (4.12) are plotted in Figures 4.5 and 4.6 for Case1 and Case 2, respectively. The two methods match well for frequencies up to a certain range. Since the dispersion-curve-matching method gives the exact dispersion relation of the lattice model, it is seen that the dynamic behavior near the band gap can be captured accurately by the corresponding effective continuum.

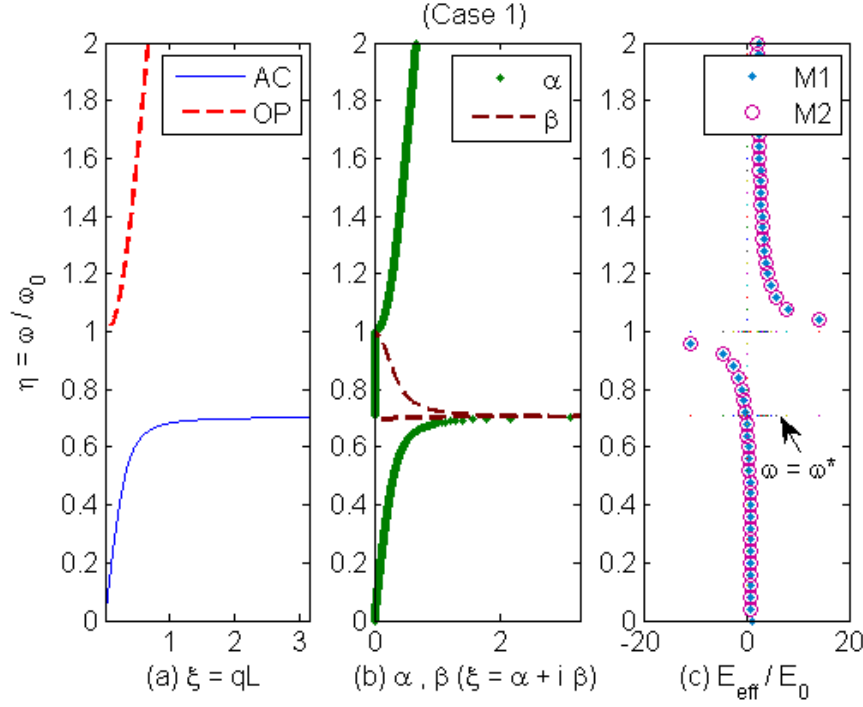


Figure 4.5 Results for case 1. (a) Dispersion relation (AC: acoustic mode; OP: optical mode); (b) attenuation factor; (c) effective modulus obtained by (M1) dynamic stiffness equivalence method of a unit, and by (M2) matching of dispersion curves.

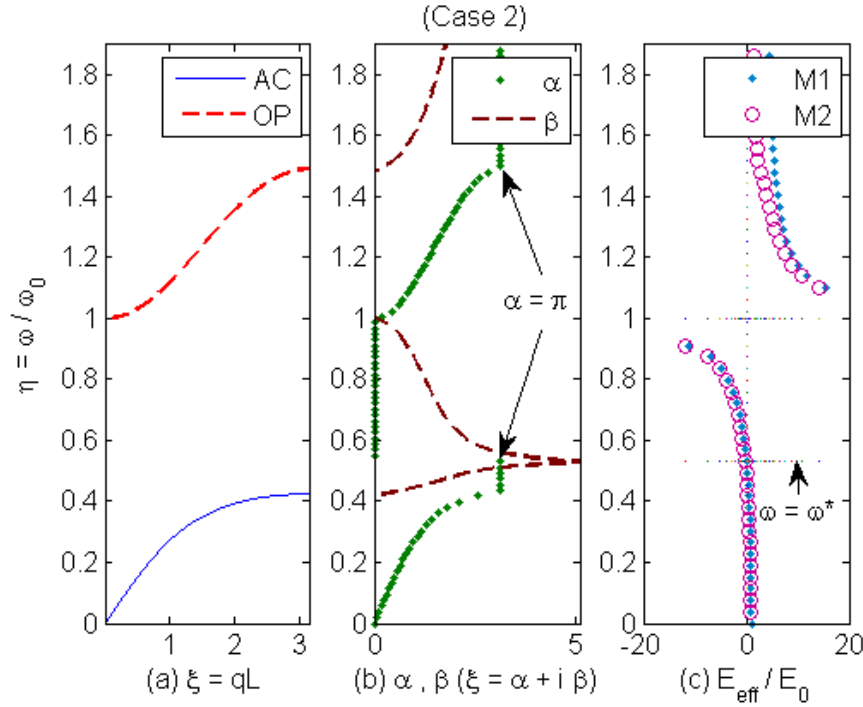


Figure 4.6 Results for case 2. (a) Dispersion relation (AC: acoustic mode; OP: optical mode); (b) attenuation factor; (c) effective modulus obtained by (M1) dynamic stiffness equivalence method of a unit, and by (M2) matching of dispersion curves.

#### 4.3.2 Mechanism of maximum wave attenuation

Of particular interest is the mechanism of maximum wave attenuation that occurs at the frequency  $\omega = \omega^*$ . Let us consider a unit of the lattice shown in Figure 4.7. One side of the unit is hinged and the other side is subjected to an excitation force  $F$ . The equations of motion for the system are:

$$(m_1/2)\ddot{u}_1 = -k_1 u_1 - 2T_1 + F \quad (4.13)$$

$$m_2\ddot{v}_2 = k_2(v_1 - v_2) \quad (4.14)$$

where  $T_1$  is the horizontal component of axial force  $T$  in the massless rigid truss member. From Figure 7, it is readily seen that

$$R = k_1 u_1 + 2T_1 \quad (4.15)$$

$$T_1 = \frac{L}{D} T_2 = \frac{L}{2D} k_2 (v_2 - v_1) \quad (4.16)$$

in which  $T_2$  is the vertical component of  $T$ .

In the following analysis, the geometrical relationship,  $v_1 = -\frac{L}{2D} u_1$ , which is valid for small displacement, is adopted. For steady state harmonic motions,  $F = \hat{F}e^{i\omega t}$ ,  $u_1 = \hat{u}_1 e^{i\omega t}$ , and  $v_2 = \hat{v}_2 e^{i\omega t}$ , and from equations (4.13- 4.14) we obtain

$$\begin{Bmatrix} \hat{u}_1 \\ \hat{v}_2 \end{Bmatrix} = \frac{\hat{F}}{\Delta} \begin{Bmatrix} -m_2\omega^2 + k_2 \\ -\frac{k_2}{2} \frac{L}{D} \end{Bmatrix} \quad (4.17)$$

where  $\Delta = \frac{1}{2} m_1 m_2 \omega^4 - \left[ \frac{1}{2} m_1 k_2 + m_2 k_1 + \frac{1}{2} m_2 k_2 (L/D)^2 \right] \omega^2 + k_1 k_2$ . The time-independent reaction force  $\hat{R}$  is obtained by substituting equation (4.17) into equations (4.15- 4.16) and using equation (4.7). We have

$$\frac{\hat{R}}{\hat{F}} = \frac{m_2 k_1 (1 + \delta\mu/2)}{\Delta} [-\omega^2 + \omega^{*2}] \quad (4.18)$$

It is noted that at frequency  $\omega = \omega^*$ ,  $\Delta \neq 0$ , but reaction force  $\hat{R} = 0$ . In other words, no force is generated at the far side of the unit. This explains why at this frequency this lattice yields the maximum wave attenuation.

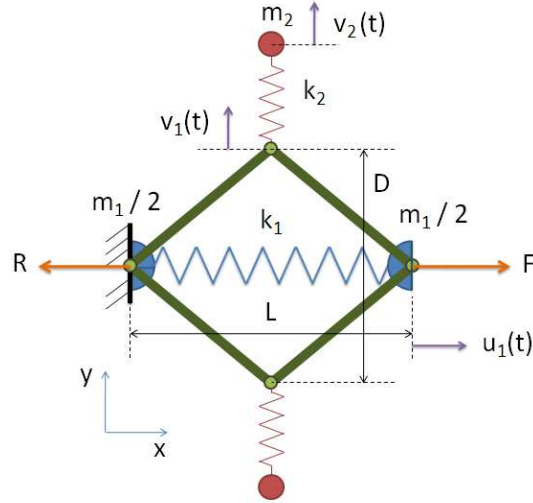


Figure 4.7 A single unit of the 1D lattice model

#### 4.3.3 Possible practical designs

One question arisen is how to practically realize acoustic metamaterials with negative elastic modulus. In Figure 8, we schematically illustrate one of the possible designs of acoustic metamaterials with frequency-dependent elastic modulus. This design take directly the form of a host material embedded with microstructures of the kind shown in Figure 1. The spring,  $k_1$ , now represents the stiffness of the base material. Another possibility is shown in Figure 9. A base plate is employed and attached with wavy springs. Concentrated masses are placed on top of the wavy springs, and, as a whole, forming the lateral local resonators. More creative designs are possible. However, details are beyond the scope of the present study.

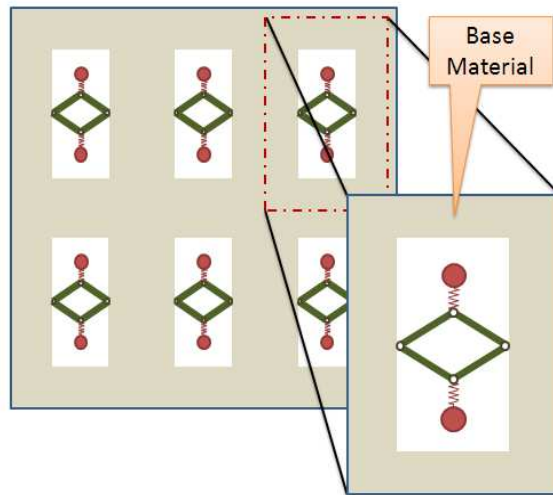


Figure 4.8 1<sup>st</sup> possible design of metamaterial with frequency-dependent effective modulus

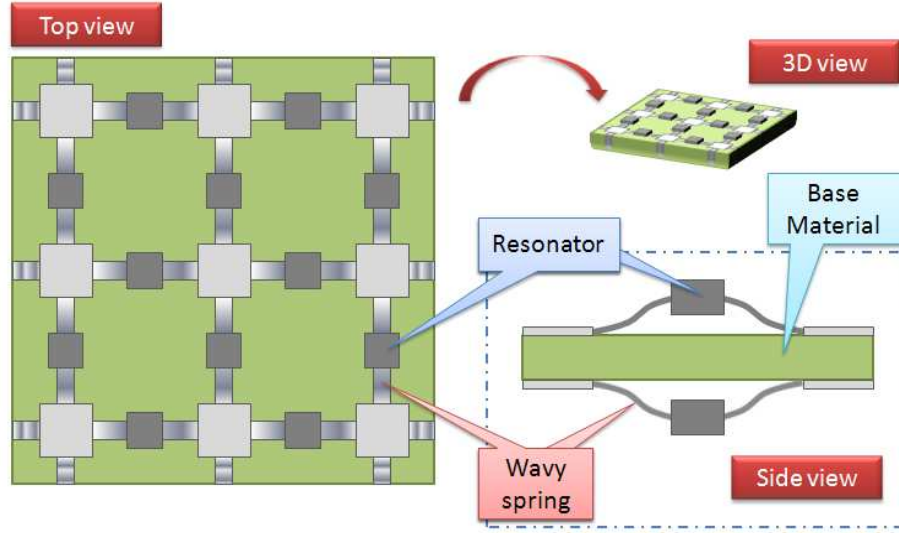


Figure 4.9 2<sup>nd</sup> possible design of metamaterial with frequency-dependent effective modulus

#### 4.4 Dynamic behavior of the metamaterial

##### 4.4.1 Semi-infinite 1D system

Using the finite element method we perform a series of numerical simulations of sinusoidal wave propagation in a 1D system (see Figure 4.4). With a large number of lattice units to prevent the reflection of waves, the system can be considered semi-infinite. Numerical results are obtained using the commercial finite element code ABAQUS Explicit. The material constants of Case 2 in Section 4.3.1 are chosen so that  $\omega^* = 0.5345\omega_0$ . The truss members are assigned with a high stiffness and low mass relative to the springs and point masses so that they can be regarded as rigid truss members. A transient harmonic excitation  $F = F_0 \sin \omega t$ ,  $t \geq 0$ , is applied at one end of the lattice system. Various input frequencies are considered.

##### 4.4.1.1 Extreme effective moduli

It is of interest to study the dynamic stress-strain relation at the first unit when the lattice system is excited by an external force. The time histories of the stress-strain curves are plotted in Figure 8. Six cases with different excitation frequencies are demonstrated.

In the figure the horizontal axis denotes non-dimensional strain  $\epsilon^{(j)} / \epsilon_0$  of the first unit, in which  $\epsilon_0$  is the strain when force  $F_0$  is applied statically, and

$$\epsilon^{(j)}(t) = [u_1^{(j)}(t) - u_1^{(j+1)}(t)] / L \quad (4.19)$$

where  $\epsilon^{(j)}$  is the strain for the  $j^{\text{th}}$  unit, and  $u_1^{(j)}$  is the displacement of  $m_1$  at the  $j^{\text{th}}$  unit. In Figure 4.10, the vertical axis is the non-dimensional stress produced by the external force. In the figure, an orange dashed-line denotes the entire response during the simulation

time window while a blue solid line shows the last few cycles of the response. It is evident that due to the transient effect, the orange dashed lines appear irregular initially but converges to the steady-state response after a number of cycles of loading. We particularly note the dynamic characteristics of the first lattice unit ( $j = 1$ ) when it exhibits an extreme effective modulus. As the excitation frequency approaches the local resonance frequency  $\omega_0$ , the dynamic effective modulus of the unit becomes very large, resulting in small strains. On the other hand, the effective modulus becomes small as the excitation frequency is near  $\omega^*$ .

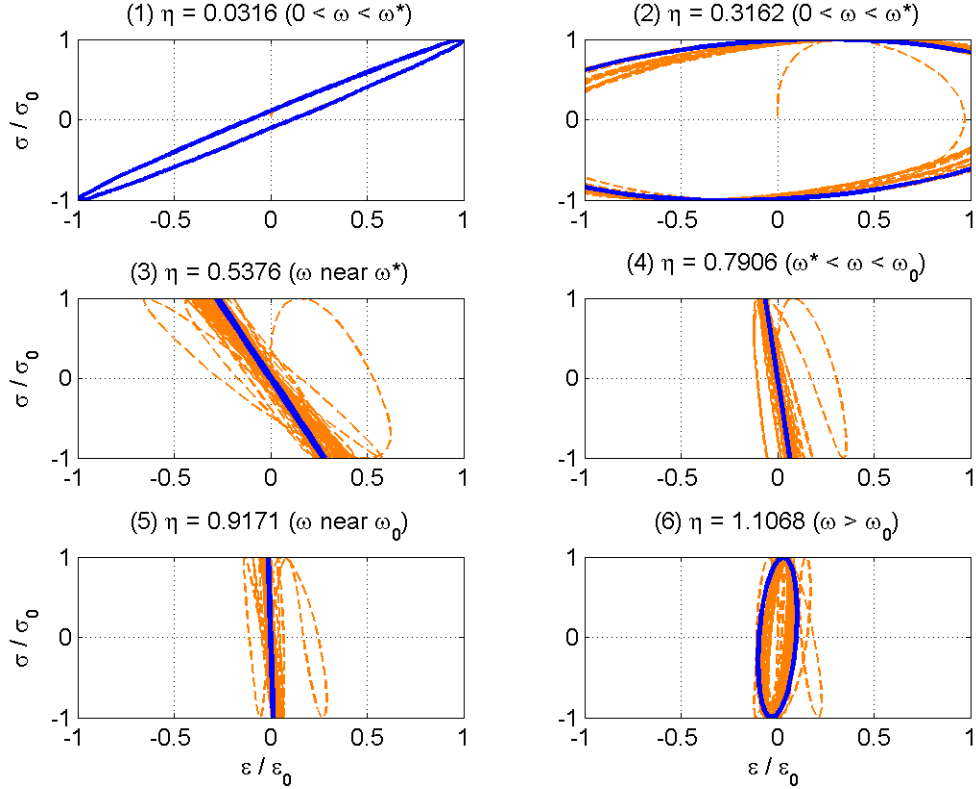


Figure 10 Various time history responses of the stress-strain relations of the first lattice unit for different excitation frequencies. Orange dashed-lines represent the entire responses of the simulation time window. Blue solid lines show responses for the last few cycles of loading.

#### 4.4.1.2 Spatial wave attenuation

It is shown in Figures 5c and 6c that, for waves with frequencies in the band gap, the dynamic effective modulus becomes negative. To further understand the mechanics of negative modulus, we perform numerical simulations for frequencies inside and outside the band gap. We measure the attenuation of wave amplitude by considering the ratio of strains in the  $j^{\text{th}}$  lattice unit and  $(j+n)^{\text{th}}$  unit as

$$\left| \frac{\mathcal{E}^{(j+n)}}{\mathcal{E}^{(j)}} \right| = \left| \frac{\max(u_1^{(j+n)} - u_1^{(j+n+1)})}{\max(u_1^{(j)} - u_1^{(j+1)})} \right| \quad (4.20)$$

Figure 4.11 shows the results for the first six lattice units for various frequencies. The three cases,  $\eta = 0.0316, 0.3162, 1.1068$ , are propagation modes while  $\eta = 0.5376, 0.7906, 0.9171$ , are attenuation modes. It is clear that the wave amplitude decays spatially when the wave frequency is in the band gap, especially when it is near  $\omega^*$ .

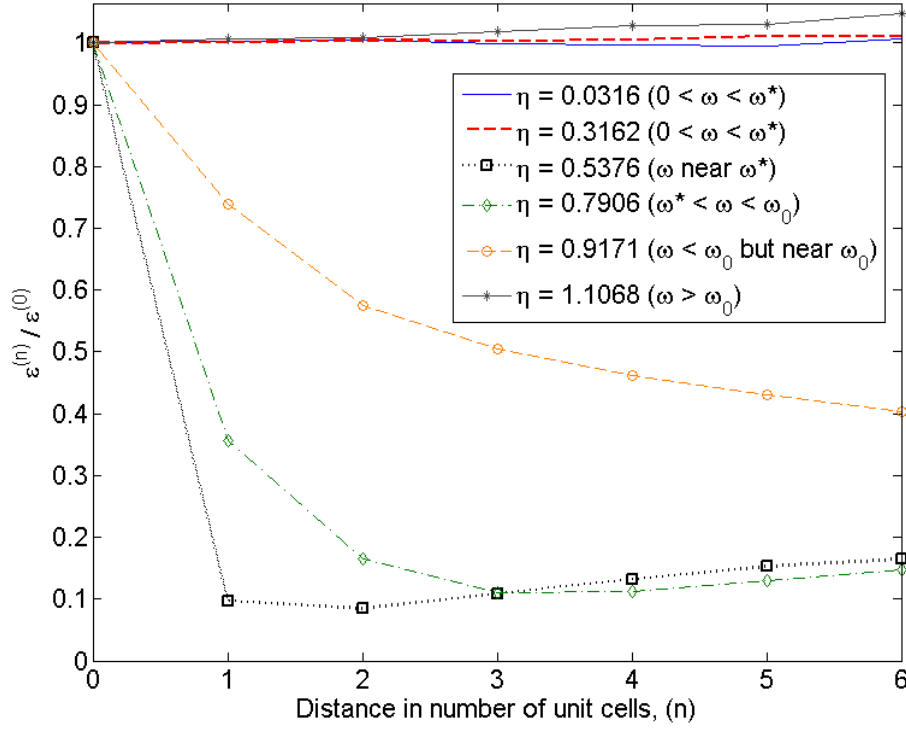


Figure 4.11 Dimensionless strain envelopes of propagating wave fields in various frequencies.  $\omega_0$  is the local resonance frequency;  $\omega^*$  is defined in equation (7);  $\epsilon^{(n)}$  represents the strain of the  $n^{\text{th}}$  unit.

#### 4.4.2 A metamaterial sandwiched between two elastic media

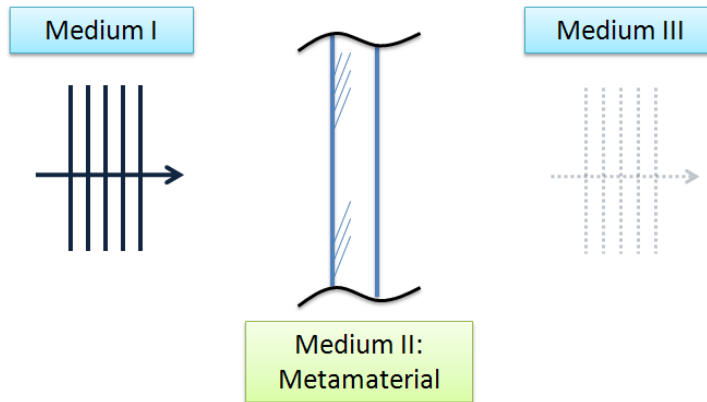


Figure 4.12 A simple illustration showing wave propagation through a metamaterial



sandwiched between two elastic media

In this section we perform numerical simulations of transient wave propagation through a metamaterial (Medium II) sandwiched between two media (Medium I and III) as depicted in Figure 4.12. This example is to further demonstrate the wave blocking and filtering capability of the present metamaterial. Using a representative 1D mass-spring lattice system (see Figure 4.4), we choose twelve units for the metamaterial in the  $x$  (longitudinal) direction. Each unit has the dimension in the  $x$  direction equal to 20 mm so that the total thickness of the metamaterial in this direction is 0.24 m. The twelve units are divided into four sections with different units of properties. In other words, the unit resonators in each section are identical but differ among different sections. We select the material parameters and corresponding frequencies,  $\omega_0$  and  $\omega^*$ , of each section as listed in Table 4.1 with  $m_1 = 2.4e-5 \text{ kg}$  and  $k = 1.75e5 \text{ N/m}$ . The resulting band gap of the designed metamaterial is covered from approximately 4100 Hz to 7550 Hz.

For simplicity and without loss of generality, we employ a simple spring-mass lattice system to represent Medium I and Medium III. In the simulation, the mass and the spring of this representative lattice are assumed to be  $m = 2.0e-5 \text{ kg}$  and  $k = 1.1e5 \text{ N/m}$ , respectively. The lattice constant is  $l = 20 \text{ mm}$ .

Table 4.1 Material constants and the corresponding frequencies of microstructures in each section of the sandwiched metamaterial

Section	1	2	3	4
$\theta$	1.667	2.000	2.500	3.000
$\delta$	0.514	0.457	0.429	0.371
$\mu$	1.778	1.778	1.778	1.778
$\omega_0$ (Hz)	7550	6500	5630	4785
$\omega^*$ (Hz)	6255	5480	4790	4145

A wave packet with an assigned central frequency is sent from the far side to the left of Medium I with a displacement-controlled excitation. The central frequency of the wave packet can be selected so that its frequency spectrum falls inside or outside the band gap. Two cases are considered. In the first case, the wave packet with the central frequency 3185 Hz is generated. The frequency band starts roughly from 2500 Hz to 4100 Hz so that it does not contain frequencies in the band gap of the metamaterial. Snapshots of the wave packet at  $t = 0.005 \text{ sec}$  and  $t = 0.050 \text{ sec}$  are shown in Figure 4.13.  $D^*$  denotes the non-dimensionalized amplitude of the displacement with respect to the maximum displacement of the input pulse. It is obvious that the wave packet propagates through the metamaterial nearly without changing in shape and amplitude. A small amount of reflection is due to the small impedance mismatch. This can also be observed from the frequency spectra of the incident and transmitted waves shown in Figure 4.14.

In the second case, the wave packet with the central frequency 5900 Hz is generated. The frequency band is roughly from 4100 Hz to 7500 Hz. Thus, it covers the band gap of the metamaterial. The snapshots at  $t = 0.005 \text{ sec}$  and  $t = 0.050 \text{ sec}$  are shown in Figure 4.15. It is evident that a large portion of the wave packet is reflected by the metamaterial and only a small portion of the wave is transmitted into the Medium III. Moreover, the frequency spectra of the incident and transmitted waves of the second case are shown in

Figure 4.16. It is observed that a large amount of frequency content is not transmitted. Using the frequency defined in equation (7) and calculated in Table 4.1 for each section, we denote  $\omega^*_j$  in the figure where “ $j$ ” is the section number of the sandwiched metamaterial. It is seen that the frequencies with maximum wave attenuation match well with those defined by equation (4.7).

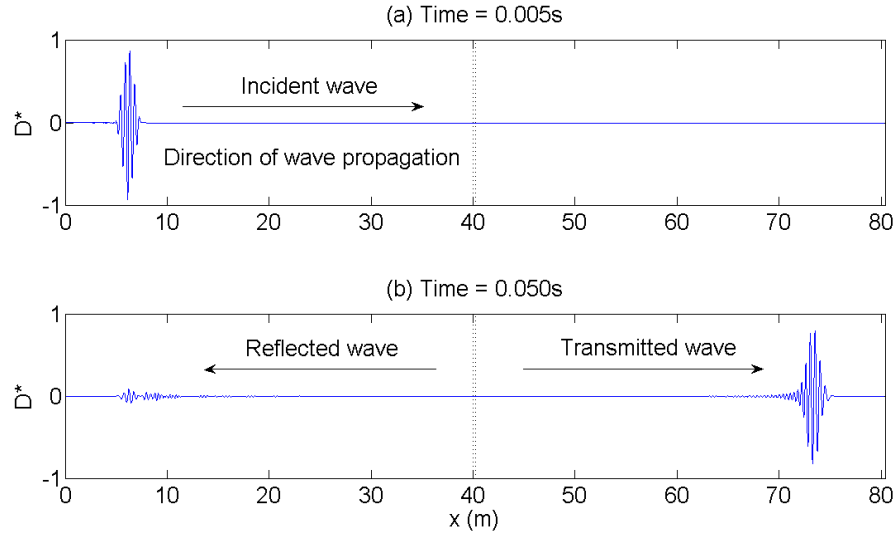


Figure 4.13 Snapshots of the wave packet with a central frequency of 3185 Hz (outside the band gap of the metamaterial) (a) before and (b) after it propagates through the metamaterial. The metamaterial is located at  $x = 40.00 \sim 40.24$  m

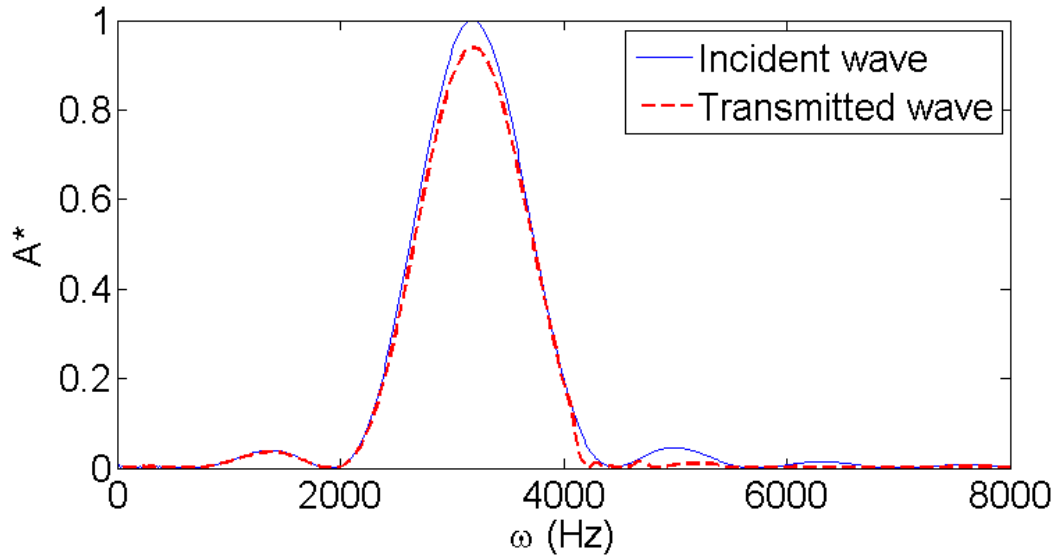


Figure 4.14 Frequency spectra of the wave packet with a central frequency of 3185 Hz at certain positions in the fluid-like media for (a) incident wave and (b) transmitted wave

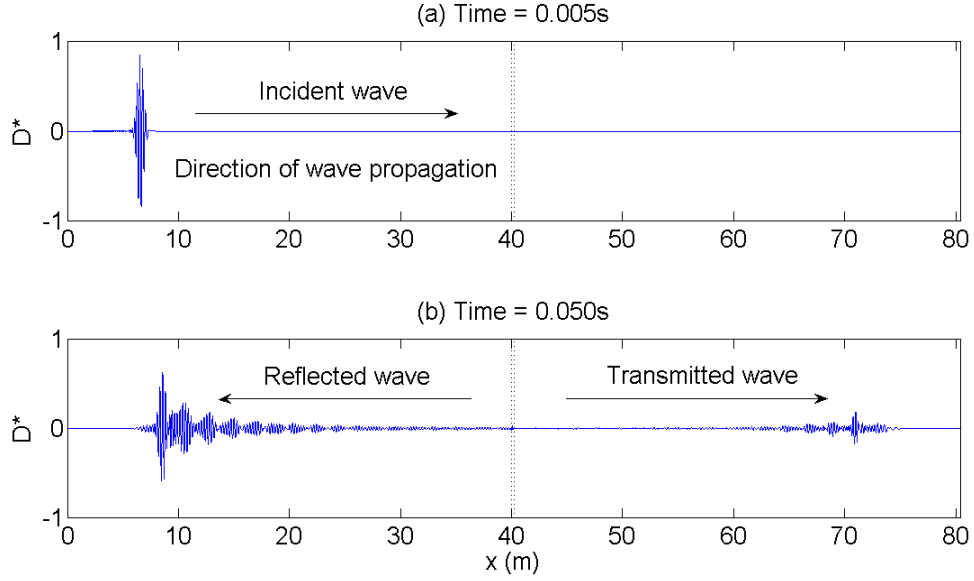


Figure 4.15 Snapshots of the wave packet with a central frequency of 5900 Hz (a) before and (b) after it propagates through the metamaterial

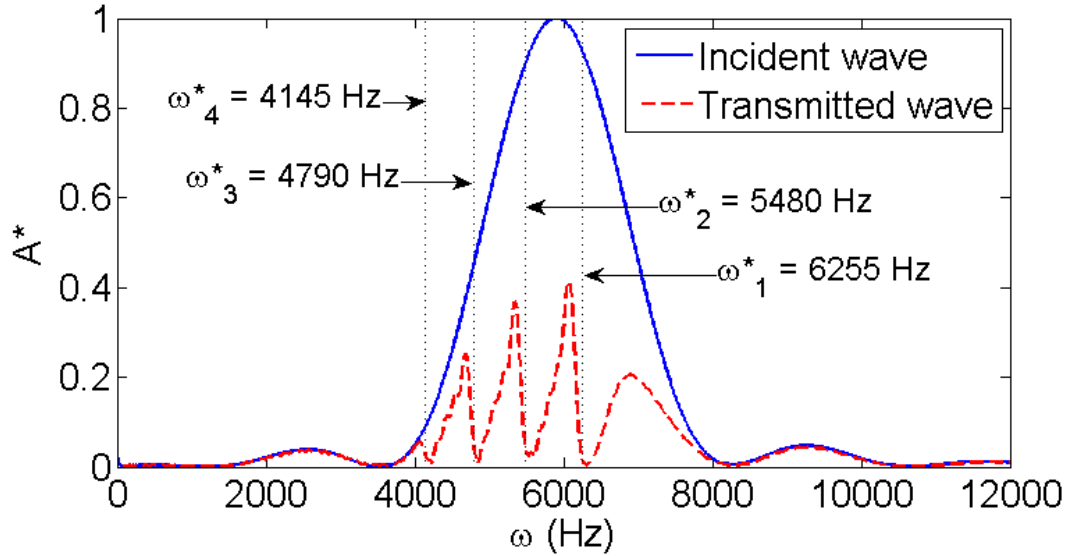


Figure 4.16 Frequency spectra of the wave packet with a central frequency of 5900 Hz at certain positions in the fluid-like media for (a) incident wave and (b) transmitted wave. Frequency defined in Eq. (7) and calculated in Table 1 for each section is denoted as  $\omega_j^*$ , where  $j$  is the section number of the sandwiched metamaterial.

#### 4.5 Conclusion

We have proposed a “microstructural” model that can be used to form an acoustic metamaterial exhibiting unusual dynamic mechanical behavior. It was shown that the

effective Young's modulus of the acoustic metamaterial is frequency-dependent and can become theoretically unbounded or vanishingly small at certain frequencies. Moreover, in certain frequency range, a band gap is created in which the effective Young's modulus becomes negative. Using a 1D system consisting of a large number of the aforementioned microstructural units, we demonstrated through numerical simulations these novel dynamic characteristics. This confirms that it is possible to create metamaterials by design of artificial microstructures to achieve certain unusual mechanical properties that are not usually present in natural materials. By combining the present model with the existing acoustic metamaterials with negative effective mass density, acoustic metamaterials having simultaneously negative effective mass density and negative effective Young's modulus can be realized.

## **5. Wave Propagation in an Acoustic Metamaterial Having Simultaneous Negative Mass Density and Young's Modulus**

### **5.1 Introduction**

For the substances having simultaneously negative electric permittivity ( $\epsilon$ ) and magnetic permeability ( $\mu$ ), many unusual properties like reverse Doppler effect, reverse Cherenkov radiation, and negative index of refraction, may arise (Veslago, 1968). The idea has been that when both  $\epsilon$  and  $\mu$  are negative, the metamaterial sustain waves with group velocity opposite to the phase velocity, and the waves can still propagate in such media without attenuation.

Similar phenomena may apply to the counterpart acoustic metamaterials owing to the mathematical analogy between acoustic and electromagnetic waves. Theoretical or experimental attempts have been made for investigation of acoustic metamaterials possessing, for instance, negative effective mass density (Liu et al., 2000; Liu et al.; Milton and Willis, 2009; Yao et al., 2008; Huang et al., 2009; Huang and Sun, 2009; Huang and Sun, 2011; Lee et al., 2009a, Islam and Newas, 2012), or negative effective elastic modulus Fang et al., 2006; Lee et al., 2009b; Huang and Sun, 2011), or both simultaneously (Li and Chan, 2004; Ding et al. 2007; Cheng et al., 2008; Lee et al., 2010; Fok and Zhang, 2011; Hu et al., 2011). For metamaterials with double negativity, the consequence is, as mentioned, metamaterial behavior of negative refraction, and, equivalently, negative phase-velocity and backward-wave phenomena (Veslago, 1968; Lakhtakia, et al., 2002; Lindell et al., 2001; Aydin and Guvan, 2005). Nevertheless, it has been shown that the negative refraction can be achieved not only by metamaterials with double negative properties, but also by Bragg scattering in periodic lattices (Notomi, 2000) and others (Chen, 2008; Ao and Chan, 2010). The similarity between these mechanisms relies on negative slope of dispersion curves in the first quadrant of dispersion relation.

According to the definition, the negative slope of the dispersion curves has been related to negative group velocity in anomalous dispersion. However, as we agree with some references, and as it will be shown in the present study, the term "negative phase velocity" is better describing the negative slope of the dispersion curves than "negative group velocity", at least for the acoustic metamaterials with double negativity. It also distinguishes the aforementioned metamaterials from the negative group-velocity media

resulting in fast-light phenomena (Wang et al., 2000; Boyd and Gauthier, 2002; Feigenbaum, 2009; Boyd and Gauthier, 2009). It is noted that the subject of the negative phase velocity has, surprisingly, been discussed since, at least, 1904 by Lamb (Lamb, 1904), using mechanical models, and by Schuster (Schuster, 1904) in electromagnetism. At that time, the researchers were pessimistic about the physical applications.

The study of EM waves in anomalous dispersion has been extensively carried out by researchers in recent years, but that of acoustic and elastic waves receives much less attention. In the present study we propose a one-dimensional (1D) elastic mass-spring system consisting of material units exhibiting simultaneously negative effective mass density and effective elastic modulus in a spectral band. The local resonance acts as the central mechanisms of the unusual behavior. Special attention is focused on the frequency band exhibiting negative slope of the dispersion curves. Transient wave propagation is investigated computationally to better understand the dynamic characteristics regarding negative phase velocity.

## 5.2 Theoretical models of acoustic metamaterials

### 5.2.1 Model of negative mass density (NMD)

Let us begin with the mass-in-mass lattice model that has been discussed by Huang and Sun (2009). As illustrated in Figure 1a, the mass-in-mass unit takes the form of a rigid ring with mass  $m_1$  which is connected to the neighboring units by springs with spring constant  $k_1$ . The ring contains an internal mass  $m_2$  connected to the ring by an internal spring with spring constant  $k_2$ . Both  $m_1$  and  $m_2$  are only allowed to move in the  $x$  (horizontal) direction.

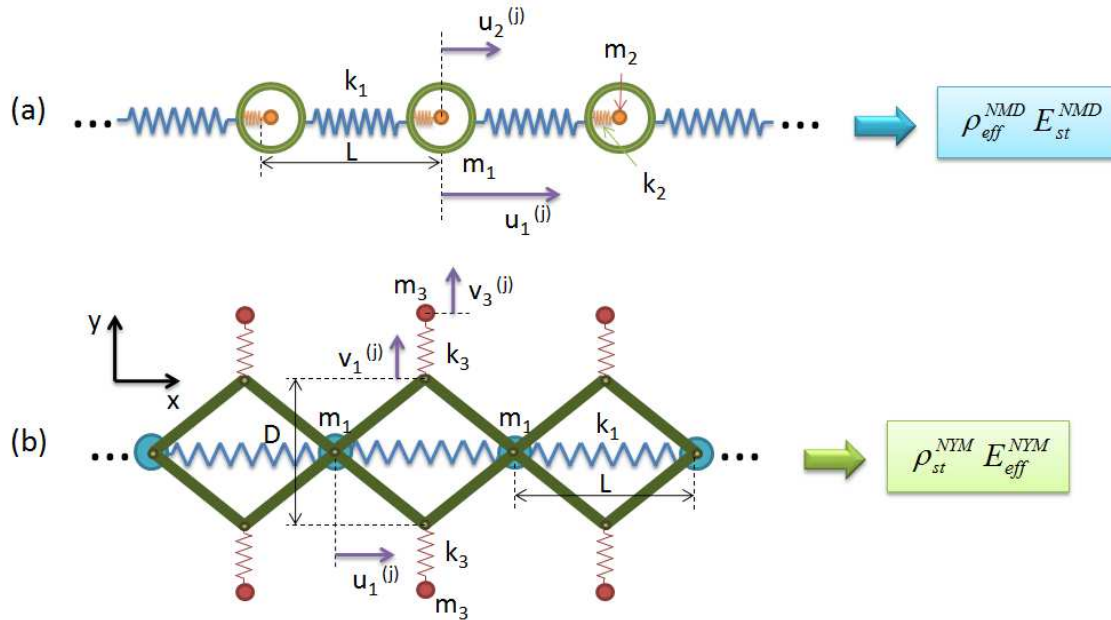


Figure 5.1 (a) One-dimensional lattice model and the continuum representative having negative effective mass density (NMD); and (b) One-dimensional lattice model and the continuum representative having negative effective Young's modulus (NYM).

The equation of motion for the  $j^{th}$  unit cell are given by

$$m_1 \frac{d^2 u_1^{(j)}}{dt^2} + k_1 (2u_1^{(j)} - u_1^{(j-1)} - u_1^{(j+1)}) + k_2 (u_1^{(j)} - u_2^{(j)}) = 0 \quad (5.1)$$

$$m_2 \frac{d^2 u_2^{(j)}}{dt^2} + k_2 (u_2^{(j)} - u_1^{(j)}) = 0 \quad (5.2)$$

where  $u_\gamma^{(j)}$  ( $\gamma = 1$  and  $2$ ) denotes the displacement of mass ' $\gamma$ ' in the  $j^{\text{th}}$  cell. The harmonic wave solution for the  $(j+n)^{\text{th}}$  unit is expressed by

$$u_\gamma^{(j+n)} = \tilde{u}_\gamma e^{i(\xi X^* + n\xi - \eta T^*)} \quad (5.3)$$

In Eq. (3),  $\xi = qL$  is the non-dimensional wavenumber,  $\eta = \omega / \omega_0^{NMD}$  the non-dimensional wave frequency,  $\omega_0^{NMD} = \sqrt{k_2 / m_2}$  the local resonance frequency,  $X^* = x / L$  the non-dimensional spatial parameter with the lattice spacing  $L$ , and  $T^* = \omega_0^{NMD} \cdot t$  the non-dimensional time. The dispersion relation is obtained by substituting the harmonic displacements in Eq. (5.3) and solving the resulting eigen-value problem of the coefficients. We obtain

$$\begin{aligned} G_{latt}^{NMD}(\eta = \omega / \omega_0^{NMD}, \xi = qL) \\ = \eta^4 - \left[ (1 + \theta_{21}) + \frac{2\theta_{21}}{\delta_{21}} (1 - \cos \xi) \right] \eta^2 + \frac{2\theta_{21}}{\delta_{21}} (1 - \cos \xi) = 0 \end{aligned} \quad (5.4)$$

where  $\theta_{21} = m_2 / m_1$  and  $\delta_{21} = k_2 / k_1$  are the non-dimensional mass ratio and stiffness ratio, respectively.

An effective elastic solid was developed by Huang and Sun (2011b) to represent the original mass-in-mass lattice. It was found that the effective mass density of the equivalent elastic solid is frequency-dependent in the form

$$\rho_{eff}^{NMD} = \rho_{st}^{NMD} \left( 1 + \frac{\theta_{21}}{1 + \theta_{21}} \frac{\eta^2}{1 - \eta^2} \right) \quad (5.5)$$

where  $\rho_{st}^{NMD} = (m_1 + m_2) / AL$  is the static mass density in which  $A$  and  $L$  are the cross-sectional area and the lattice spacing, respectively. This model is denoted as “NMD” since it exhibits negative effective mass density in the range

$$1 < \eta = \frac{\omega}{\omega_0^{NMD}} < \sqrt{1 + \theta_{21}} \quad (5.6)$$

The time-independent wave equation for plane harmonic waves is simply given by

$$-\rho_{eff} \omega^2 \hat{u} = E_{eff} \frac{\partial^2 \hat{u}}{\partial x^2} \quad (5.7)$$

where the effective mass density  $\rho_{eff} = \rho_{eff}^{NMD}$  is given in Eq. (5.5), and the effective Young's modulus,  $E_{eff} \equiv E_{st}^{NMD} \equiv k_1 L / A$ , is determined from the static stress-strain relation.

The harmonic wave solution for the equivalent elastic solid is given by  $\hat{u} = \tilde{u}e^{i\xi x^*}$ . Hence the dispersion relation is obtained as

$$G_{\text{elast}}^{NMD}(\eta, \xi) = \rho_{\text{eff}}^{NMD} (\omega_0^{NMD})^2 \eta^2 - E_{\text{st}}^{NMD} \xi^2 / L^2 = 0 \quad (5.8)$$

### 5.2.2 Model of negative Young's modulus (NYM)

Next we consider the mechanical lattice model having lateral local resonators shown in Figure 5.1b. This model was investigated and discussed by Huang and Sun (2011a). Briefly, point masses  $m_1$  are connected by springs with a spring constant  $k_1$ . Four rigid and massless truss members are assembled symmetrically as shown to support two sets of microstructures consisting of springs with spring constant  $k_3$  and masses  $m_3$ . Point mass  $m_3$  is allowed to move only in the  $y$  (vertical) direction.  $L$  and  $D$  are geometrical parameters shown in the figure.

For this lattice model, the equations of motion for the  $j^{\text{th}}$  unit are given by

$$m_1 \frac{d^2 u_1^{(j)}}{dt^2} + k_1 (2u_1^{(j)} - u_1^{(j-1)} - u_1^{(j+1)}) + 2k_3 (v_3^{(j-1)} - v_1^{(j-1)}) \left( \frac{L}{2D} \right) - 2k_3 (v_3^{(j)} - v_1^{(j)}) \left( \frac{L}{2D} \right) = 0 \quad (5.9)$$

$$m_3 \frac{d^2 v_3^{(j)}}{dt^2} + k_3 (v_3^{(j)} - v_1^{(j)}) = 0 \quad (5.10)$$

From geometrical relations based on the assumption of small displacements, we have

$$v_1^{(j)} = -\frac{(2L - \Delta u_1^{(j)}) \Delta u_1^{(j)}}{4D} + \frac{(2L - \Delta u_1^{(j)})^2 (\Delta u_1^{(j)})^2}{16D^3} + \dots \\ \approx -\frac{L}{2D} \Delta u_1^{(j)} = -\frac{L}{2D} (u_1^{(j+1)} - u_1^{(j)}) \quad (5.11)$$

In a similar manner, the dispersion relation is obtained as

$$G_{\text{latt}}^{NYM}(\bar{\eta} = \omega / \omega_0^{NYM}, \xi = qL) \\ = \bar{\eta}^4 - \left[ 1 + \frac{2\theta_{31}}{\delta_{31}} \left( 1 + \frac{\delta_{31}\mu}{2} \right) (1 - \cos \xi) \right] \bar{\eta}^2 + \frac{2\theta_{31}}{\delta_{31}} (1 - \cos \xi) = 0 \quad (5.12)$$

where  $\theta_{31} = m_3 / m_1$ ,  $\delta_{31} = k_3 / k_1$ ,  $\bar{\eta} = \omega / \omega_0^{NYM}$ ,  $\omega_0^{NYM} = \sqrt{k_3 / m_3}$ , and  $\mu = (L / D)^2$ . The relation of the non-dimensional wave frequencies reads

$$\bar{\eta} = \eta \sqrt{(\theta_{31} \delta_{21}) / (\theta_{21} \delta_{31})} \quad (5.13)$$

If this lattice system is represented by an equivalent elastic solid, the effective Young's modulus of the solid is found frequency-dependent in the form

$$E_{\text{eff}}^{NYM} = E_{\text{st}}^{NYM} \left( 1 + \frac{\delta_{31}\mu}{2} \frac{\bar{\eta}^2}{\bar{\eta}^2 - 1} \right) \quad (5.14)$$

where  $E_{\text{st}}^{NYM} = k_1 L / A$  is the static Young's modulus. This model, denoted as "NYM", exhibits negative effective Young's modulus in the range

$$\sqrt{\frac{2}{2 + \delta_{31}\mu}} < \bar{\eta} = \frac{\omega}{\omega_0^{NYM}} < 1 \quad (5.15)$$

The wave equation takes the form of Eq. (5.7), in which the effective Young's modulus,  $E_{eff} = E_{eff}^{NYM}$ , is given by Eq. (5.14) and the effective mass density is the static formulation,  $\rho_{eff} = \rho_{st}^{NYM} = m_1 / AL$ . (Note that the masses  $m_3$  in this model are assumed to move only in the  $y$  direction so that they contribute zero inertia forces in the  $x$  direction). The dispersion relation is given by

$$G_{elast}^{NYM}(\bar{\eta}, \xi) = \rho_{st}^{NYM} (\omega_0^{NYM})^2 \bar{\eta}^2 - E_{eff}^{NYM} \xi^2 / L^2 = 0 \quad (5.16)$$

### 5.2.3 Model of double negativity (DN)

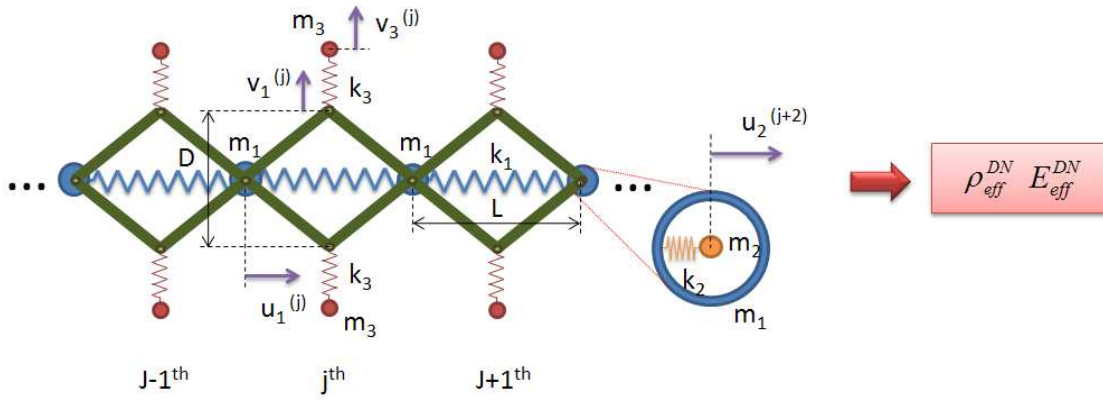


Figure 5.2 One-dimensional lattice model exhibiting double negativity (DN)

Consider a 1D infinite lattice shown in Figure 5.2. This model is a combination of the two models in Figures 5.1 such that mass  $m_1$  in the NYM model is replaced by the mass unit in NMD. This model is denoted as “DN” as it will be shown to possess double negativity. Let the displacements of masses  $m_1$ ,  $m_2$ , and  $m_3$  at the  $j^{\text{th}}$  unit be  $u_1^{(j)}(t)$ ,  $u_2^{(j)}(t)$ ,  $v_3^{(j)}(t)$ , respectively. The equations of motion of the system at the  $j^{\text{th}}$  cell are readily obtained as

$$m_1 \frac{\partial^2 u_1^{(j)}}{\partial t^2} = k_1(u_1^{(j-1)} - u_1^{(j)}) + k_1(u_1^{(j+1)} - u_1^{(j)}) + k_2(u_2^{(j)} - u_1^{(j)}) - 2k_3(v_3^{(j-1)} - v_1^{(j-1)})\left(\frac{L}{2D}\right) + 2k_3(v_3^{(j)} - v_1^{(j)})\left(\frac{L}{2D}\right) \quad (5.17)$$

$$m_2 \frac{\partial^2 u_2^{(j)}}{\partial t^2} = k_2(u_1^{(j)} - u_2^{(j)}) \quad (5.18)$$



$$m_3 \frac{\partial^2 v_3^{(j)}}{\partial t^2} = k_3 (v_1^{(j)} - v_3^{(j)}) \quad (5.19)$$

The steady-state solution of the equations of motion (5.17-5.19) is determined by letting the displacements be

$$u_1^{(j+n)} = \hat{u}_1 e^{i(\xi X^* + n\xi - \eta T^*)}, \quad u_2^{(j+n)} = \hat{u}_2 e^{i(\xi X^* + n\xi - \eta T^*)}, \quad \text{and} \quad v_3^{(j+n)} = \hat{v}_3 e^{i(\xi X^* + n\xi - \eta T^*)} \quad (5.20)$$

where, again,  $\xi = qL$  is the non-dimensional wavenumber,  $X^* = x/L$  and  $T^* = \omega_0^{NMD} \cdot t$  are the non-dimensional parameters in space and time, respectively. Substituting these harmonic displacements in Eqs. (5.17) to (5.19) and solving the resulting eigen-value problem of the coefficients, we obtain the dispersion relation:

$$\begin{aligned} G_{latt}^{DN}(\eta, \xi) = & -\eta^6 + \left\{ 1 + \frac{\delta_{31}\theta_{21}}{\delta_{21}\theta_{31}} + \frac{\theta_{21}}{\delta_{21}} \left[ 2 \left( 1 + \frac{\delta_{31}\mu}{2} \right) (1 - \cos \xi) + \delta_{21} \right] \right\} \eta^4 \\ & - \left[ (1 + \theta_{21}) \frac{\delta_{31}\theta_{21}}{\delta_{21}\theta_{31}} + 2 \frac{\theta_{21}}{\delta_{21}} \left( \frac{\delta_{31}\theta_{21}}{\delta_{21}\theta_{31}} + 1 + \frac{\delta_{31}\mu}{2} \right) (1 - \cos \xi) \right] \eta^2 \\ & + 2 \frac{\delta_{31}\theta_{21}^2}{\delta_{21}^2\theta_{31}} (1 - \cos \xi) \\ = & 0 \end{aligned} \quad (5.21)$$

On the other hand, the equation of motion of the equivalent one-dimensional elastic solid is given by Eq. (5.7). In this formulation the effective mass density and the effective Young's modulus are given by Eq. (5.5),  $\rho_{eff}^{DN} = \rho_{eff}^{NMD}$ , and Eq. (5.14),  $E_{eff}^{DN} = E_{eff}^{NYM}$ , respectively. Consequently, the dispersion relation of the representative elastic solid is obtained as

$$G_{elast}^{DN}(\eta, \xi) = \rho_{eff}^{DN} (\omega_0^{NMD})^2 \eta^2 - E_{eff}^{DN} \xi^2 / L^2 = 0 \quad (5.22)$$

### 5.3. Effective dynamic parameters and dispersion relation

For numerical illustrations, we present two cases with the following assumed material constants:

$$\begin{aligned} \text{(Case 1)} \quad & \theta_{21} = m_2 / m_1 = 1.5, \quad \theta_{31} = m_3 / m_1 = 1, \quad \delta_{21} = k_2 / k_1 = 0.1, \quad \delta_{31} = k_3 / k_1 = 1, \\ & \mu = (L/D)^2 = 2.78, \end{aligned}$$

and

$$\text{(Case 2)} \quad \theta_{21} = 2.25, \quad \theta_{31} = 0.4, \quad \delta_{21} = 0.3, \quad \delta_{31} = 0.25, \quad \mu = 25$$

As has been mentioned in Section 5.2.3, the model in Figure 5.2 is denoted as “DN” because for some range of wave frequencies it could exhibit double negativity. This range can be obtained from the negative modulus and mass density properties and their corresponding spectral regions. The effective mass density in Eq. (5.5) and the effective

Young's modulus in Eq. (5.14) with respect to the non-dimensional wave frequency for Case 1 and Case 2 are illustrated in Figures 3 and 4, respectively.

In Figure 5.3 for Case 1, the material constants are selected so that the frequency range of the negative quantity of the NMD model lies apart from that of the NYM model. In other words, for the frequency range in-between the two regions with negative quantity (e.g.,  $\eta$  approximately ranges in 1.6 and 2.5 in Figure 5.3), both the effective mass density and the effective Young's modulus are positive. On the other hand, in Figure 5.4 for Case 2, the material constants are chosen so that the frequency ranges of both negative quantities of the NMD and the NYM models overlap.

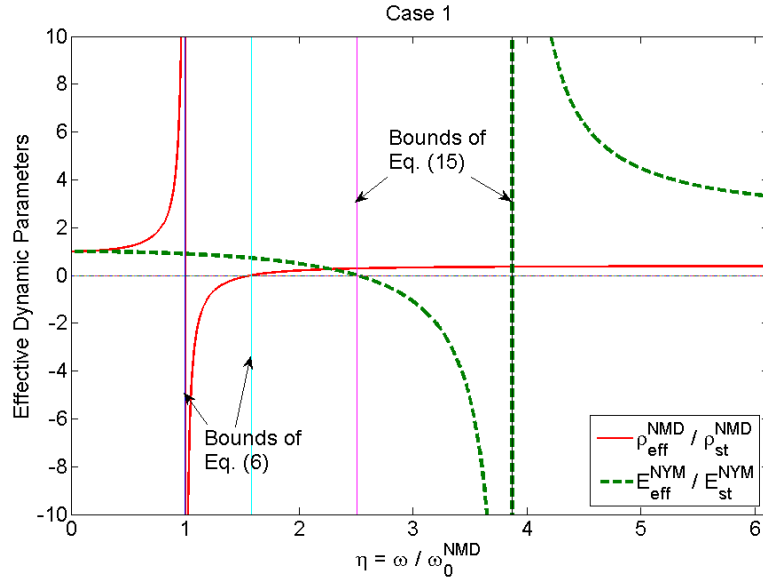


Figure 5.3 Effective dynamic non-dimensional parameters for Case 1 using Eqs. (5.5) and (5.14). The bounds of negative quantities are described in Eqs. (5.6) and (5.15).

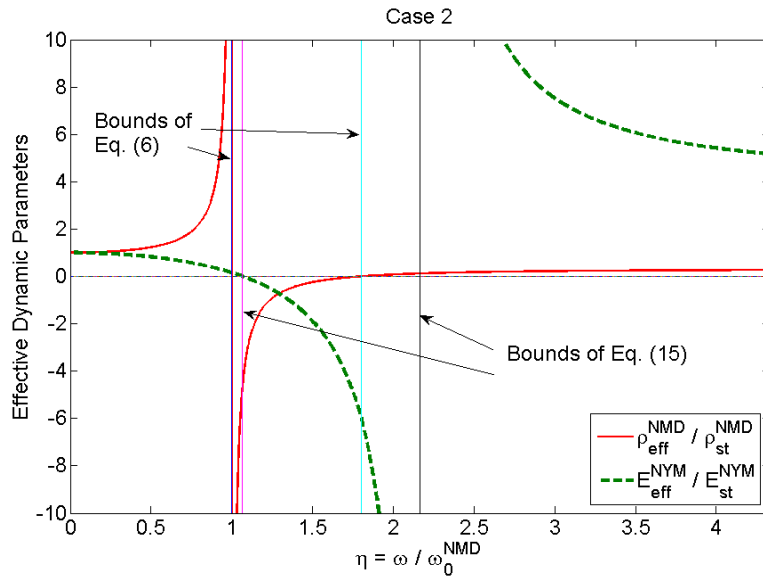


Figure 5.4 Effective dynamic non-dimensional parameters for Case 2. Descriptions are referred to the caption of Figure 5.3.

Next, the dispersion curves for both cases obtained using the exact formulation (Eqs. (5.4), (5.12), and (5.21) for NMD, NYM, and DN models, respectively) of the lattice model are shown in Figures 5.5 and 5.6, respectively, with solid lines. In each figure, three columns labeling DN, NMD, and NYM represent the dispersion curves of the double negativity model, the negative mass density model, and the negative Young's modulus model, respectively. For each diagram, band gaps, where waves attenuated and stopped, exist due to the effect of the local resonance.

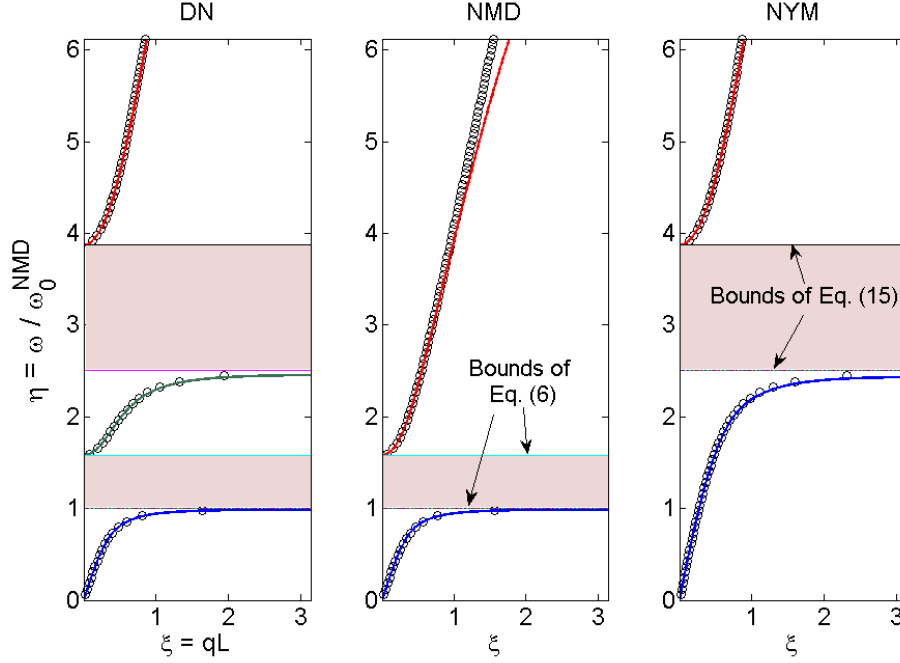


Figure 5.5 Dispersion curves for Case 1. DN: double negativity model; NMD: negative mass density model; NYM: negative Young's modulus model; *Solid lines*: mass-spring lattice model from Eqs. (4), (12), and (21) for NMD, NYM, and DN models, respectively; *Circles*: equivalent elastic solid from Eqs. (8), (16), and (22) for NMD, NYM, and DN models, respectively.

The accuracy of the elastic solid representation can be verified by comparing the dispersion curves obtained with the lattice and the elastic solid models. In Figures 5.5 and 5.6, the dispersion curves of the equivalent elastic solid are obtained using Eqs. (5.8), (5.16), and (5.22) for the NMD, NYM, and DN models, respectively. Good approximation is observed for the lower branch for all models. For the higher branch some deviation is seen at the high frequency range. The reason is that the equivalent elastic solid employs an approximate formulation from the original lattice system based on a long wavelength approximation. It is noted that the shaded areas in the figures indicate the negative properties derived from Eqs. (5.6) and (5.15) for the NMD and NYM model, respectively. For both cases and for the DN model, the band gaps closely match the shaded areas of the separate models.

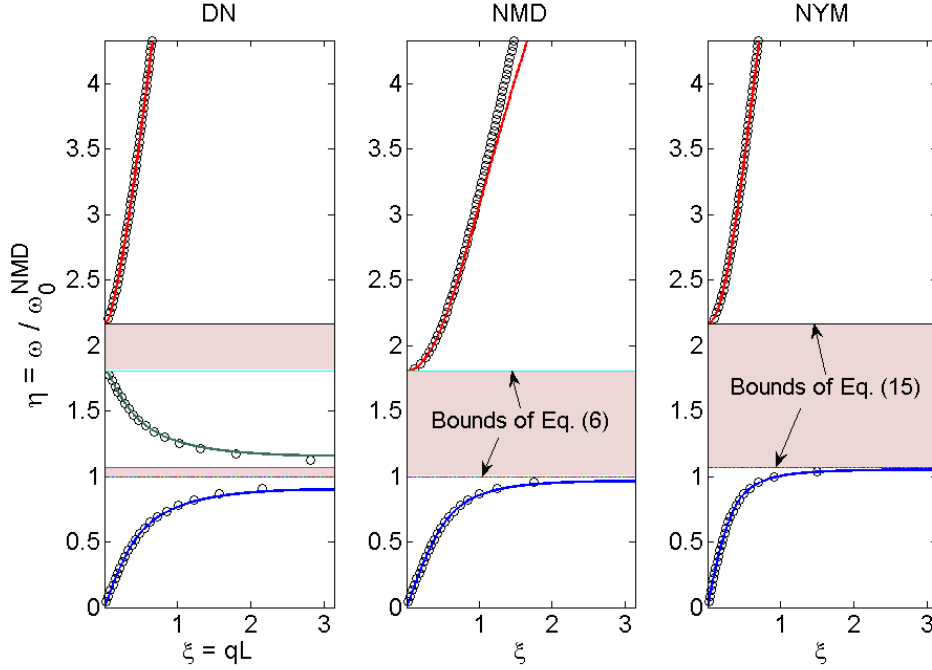


Figure 5.6 Dispersion curves for Case 2; Solid lines: mass-spring lattice model; Circles: elastic solid model; detailed description referred to Figure 5.5.

## 5.4 Phase velocity and group velocity

### 5.4.1 Phase velocity

In the present study we adopt the definition of the phase velocity of a harmonic wave as the following form

$$v_p = \frac{\omega}{q} \quad (5.23)$$

All points of the same phase propagate in space with this velocity. In the dispersion  $\omega$ - $q$  diagram, the phase velocity is given by the slope of the straight line connecting the origin and a certain point on the dispersion curve. Since negative wave frequency is not in our consideration, it is obvious that the wave vector,  $\vec{q}$ , points in the direction of phase velocity.

For an effective elastic solid of an acoustic metamaterial, the dispersion relation can be obtained by, for instance, employing Eq. (5.7) together with  $\rho_{eff}$  in Eq. (5.5) and  $E_{eff}$  in Eq. (5.14), and substituting the harmonic plane-wave solution into the Eq. (5.7). The dispersion relation reads

$$G(\omega, q) = \rho_{eff} \omega^2 - E_{eff} q^2 = 0 \quad (5.24)$$

From the dispersion relation, one can immediately conclude that in order for the elastic medium to have wave propagation without attenuation (i.e., a real solution for  $q$ ), the medium must have either both positive  $\rho_{eff}$  and  $E_{eff}$  or both negative  $\rho_{eff}$  and  $E_{eff}$ .

The phase velocity is thus given by

$$v_p = \frac{\omega}{q} = \pm \sqrt{\frac{E_{eff}}{\rho_{eff}}} \quad (5.25)$$

This is still not possible to determine the direction of a wave in the acoustic metamaterial from the sign of phase velocity, or the wave vector, based on the given dispersion relation, since the real wave vector  $q$  could be either positive or negative. We shall proceed to the next subsections for further investigation.

#### 5.4.2 Group velocity of DN acoustic metamaterial

Of particular interest is to investigate the sign of group velocity of a wave group or packet in an acoustic metamaterial. This wave group or packet corresponds to a superposition of harmonic waves with very similar wave frequencies  $\omega$  and wavenumbers  $q$ . In the dispersion  $\omega$ - $q$  diagram, the group velocity of a wave group or packet is given by the slope of the dispersion curve. By using the implicit differentiation, the final expression of the group velocity reads

$$v_g = \frac{d\omega}{dq} = -\left(\frac{\partial G}{\partial \omega}\right)^{-1} \left(\frac{\partial G}{\partial q}\right) = \frac{2E_{eff}q}{2\rho_{eff}\omega + \left(\frac{\partial \rho_{eff}}{\partial \omega} - \frac{\partial E_{eff}}{\partial \omega} \frac{\rho_{eff}}{E_{eff}}\right)\omega^2} \quad (5.26)$$

From the expressions given by Eq. (5.5) and Eq. (5.14) it can be shown that

$$\frac{\partial \rho_{eff}}{\partial \omega} = \frac{2\rho_{st}^{NMD} \lambda}{\omega_0^{NMD}} \frac{\eta}{(1-\eta^2)^2} \geq 0 \quad (5.27)$$

and

$$\frac{\partial E_{eff}}{\partial \omega} = -\frac{E_{st}^{NYM} \delta_{31} \mu}{\omega_0^{NYM}} \frac{\bar{\eta}}{(\bar{\eta}^2 - 1)^2} \leq 0 \quad (5.28)$$

where  $\lambda = \theta_{21} / (1 + \theta_{21})$ . The term  $\left(-\frac{\partial E_{eff}}{\partial \omega} \frac{\rho_{eff}}{E_{eff}}\right)\omega^2$  in the denominator in Eq. (5.26) is always positive if  $\rho_{eff}$  and  $E_{eff}$  are of the same sign. Substituting Eqs. (5.5) and (5.26) in the remainder of the denominator of Eq. (5.26),  $2\rho_{eff}\omega + \left(\frac{\partial \rho_{eff}}{\partial \omega}\right)\omega^2$ , we obtain

$$2\rho_{eff}\omega + \left(\frac{\partial \rho_{eff}}{\partial \omega}\right)\omega^2 = \frac{2\rho_{st}^{NMD} \omega}{(1-\eta^2)^2} \left[(1-\lambda)(1-\eta^2)^2 + \lambda\right] \geq 0 \quad (5.29)$$

Since  $0 \leq \lambda \leq 1$  is always true, this inequality holds for all frequencies. It is, therefore, proved that the denominator of Eq. (26) is positive for identical signs of  $\rho_{eff}$  and  $E_{eff}$ .

Obviously, from Eq. (5.26), group velocity,  $v_g$ , is proportional to  $E_{eff}q$ . The sign of group velocity is, hence, affected by the sign of the effective Young's modulus  $E_{eff}$  and the wave number  $q$ . From the last section, in order for an elastic medium to

have wave propagation without attenuation, the medium must possess either both positive  $\rho_{eff}$  and  $E_{eff}$  or both negative  $\rho_{eff}$  and  $E_{eff}$ . If  $\rho_{eff}$  and  $E_{eff}$  of the medium are both positive, group velocity  $v_g$  is obviously positive for a positive wavenumber. On the other hand, if  $\rho_{eff}$  and  $E_{eff}$  are simultaneously negative, waves, therefore, propagate in the medium with opposite signs of phase velocity  $v_p$  and group velocity  $v_g$ .

### 5.4.3 Negative phase velocity

For waves in a lossless elastic medium the energy velocity is identical to the group velocity (Brillouin, 1953). In view of positive energy flow for a lossless elastic medium, the group velocity is always positive. Once again, we exclude the negative group-velocity media resulting in fast-light phenomena. That negative group-velocity phenomenon is beyond the scope of the present study.

For the acoustic metamaterial with frequency-dependent effective mass density  $\rho_{eff}$  and Young's modulus  $E_{eff}$ , if  $\rho_{eff}$  and  $E_{eff}$  are both positive, a positive group velocity results in a positive wave number. On the other hand, if  $\rho_{eff}$  and  $E_{eff}$  are negative simultaneously, in order to have a positive group velocity, wave number must be negative. This means that in the double negativity frequency region, the sign of phase velocity  $v_p$  in Eq. (5.25) must be negative.

## 5.5 Dynamic characteristics of wave propagation by simulation

### 5.5.1 Harmonic waves

To investigate how a group of waves of essentially the same wavelength propagates with a negative phase velocity, we perform numerical simulations of transient wave propagations. One of the reasons the transient wave propagation rather than steady-state wave propagation is studied is because the direction of disturbances, hence the direction of group velocity, can be ensured.

Dynamic simulations are implemented by use of the ABAQUS Explicit solver. In each simulation, a lattice model shown in Figure 5.2 is constructed with a sinusoidal displacement,  $U(t) = U_0 \sin(\omega t) H(t)$ , applied at the left end of the lattice. The material properties of Case 2 listed in Section 3 together with  $\omega_0^{NMD} = 115.47 \text{ rad/s}$  are used. If the lattice system is long enough, the reflected wave does not appear in the window of numerical results.

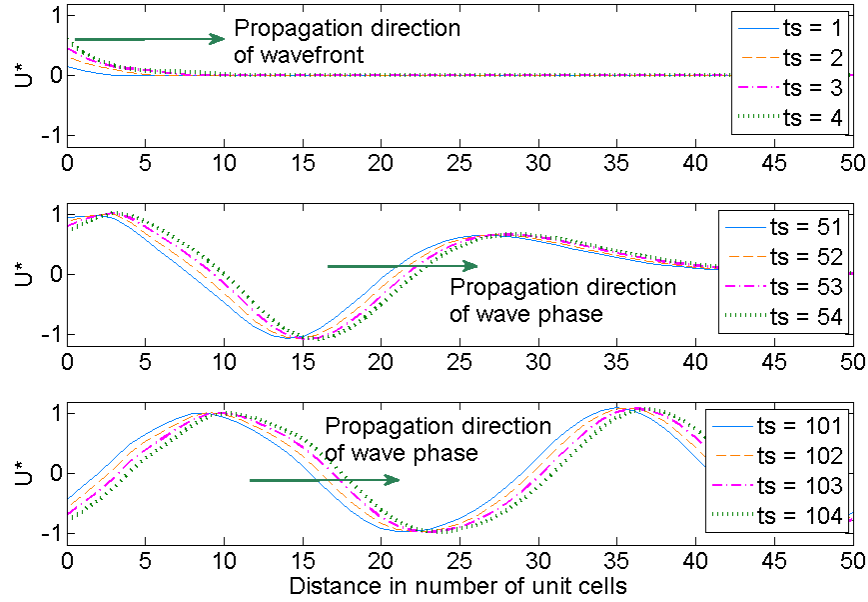


Figure 5.7 Snapshots of sinusoidal wave propagation in finite DN model with excitation frequency  $\eta = \omega / \omega_0^{NMD} = 0.346$  and  $\omega_0^{NMD} = 115.47 \text{ rad/s}$  (in the double-positivity region;  $ts$  = time step;  $T^* = \omega_0^{NMD} \cdot t = ts \cdot \Delta T^*$  with  $\Delta T^* = 0.462$ ).

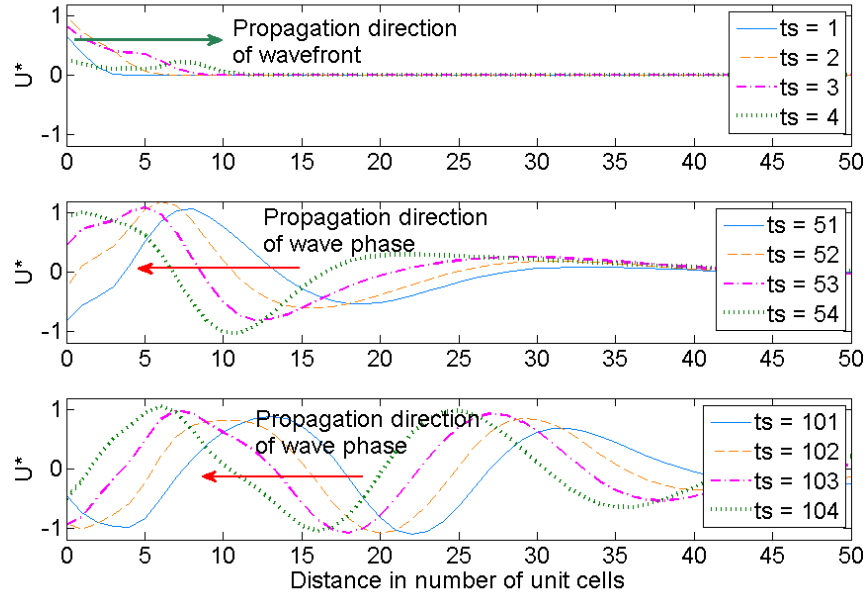


Figure 5.8 Snapshots of sinusoidal wave propagation in finite DN model with excitation frequency  $\eta = \omega / \omega_0^{NMD} = 1.559$  and  $\omega_0^{NMD} = 115.47 \text{ rad/s}$  (in the double-negativity region;  $ts$  = time step;  $T^* = \omega_0^{NMD} \cdot t = ts \cdot \Delta T^*$  with  $\Delta T^* = 0.462$ ).

Figures 5.7 and 5.8 show the snapshots of the displacement fields in space with two different wave frequencies,  $\eta = \omega / \omega_0^{NMD} = 0.346$  and 1.559, respectively.  $U^*$  denotes the normalized amplitude of the displacements with respect to  $U_0$ . In each figure, a typical propagation mode is demonstrated. Three consecutive sections of time,  $T^* = ts \cdot \Delta T^*$  with the non-dimensional time increment  $\Delta T^* = 0.462$ , show the behavior of wave propagation. For now, let us assume that the time increment  $\Delta T^*$  is sufficiently small in capturing the dynamic behavior of the model. We shall come to this point immediately in the following paragraph. Note that, again,  $T^* = \omega_0^{NMD} \cdot t$  is the non-dimensional parameter in time domain and  $t$  is in seconds. “ts” denotes the time steps hereafter. Section 1 (ts = 1~4), for instance, is the initial state and the section 3 (ts = 101~104) is considered close to steady state.

Selection of the time increment,  $\Delta T^*$ , for visualization of simulation results is nontrivial. An improper selection of the increments may, on the one hand, produce incorrect simulation results, or, on the other hand, simply cause expensive computation. Here we provide a simple guide for the balance of accuracy and efficiency. The definition of the time increment reads

$$\Delta T^* = \omega_0^{NMD} \frac{t}{ts} = \omega_0^{NMD} \cdot \Delta t \quad (5.30)$$

where  $\Delta t$  is the time step in seconds. Substituting the non-dimensional wave frequency  $\eta = \omega / \omega_0^{NMD}$  in Eq. (5.30) and use the relationship of angular frequency and period of time we obtain

$$\Delta T^* = \frac{2\pi}{\eta} \frac{\Delta t}{T_p} \quad (5.31)$$

For a harmonic wave,  $\Delta t \leq T_p / 8$  should be sufficient in capturing the dynamic behavior of the models in the present study. For Case 2, for instance, this inequality  $\Delta t \leq T_p / 8$  and the wave frequency  $\eta = 1.559$ , together with Eq. (5.31), result in  $\Delta T^* \leq 0.504$ . Clearly the time increments chosen for both cases are satisfactory.

In Figure 5.7, given the first section from ts = 1 to 4, the propagation direction of the front of the dynamic disturbance is seen pointing from left to right, indicating the direction of the energy flow. However, due to the nature of transient wave propagation, the forerunner of the dynamic disturbance may contain frequencies other than the excitation frequency  $\omega$ . Further time steps, in the middle and bottom windows of Figure 5.7, need to be carried out in order to make sure the energy direction of the sinusoidal wave with exactly the excitation frequency  $\omega$ . In the second section, ts = 51 to 54, it is seen that the transient part of the wave already propagates to the right side of the spatial window, leaving the transition to steady state at the left part of the window. From the third section, ts = 101 to 104, a more complete configuration approaching the steady-state wave propagation can be observed. At this stage, the propagation direction of the wave phase is observed pointing from left to right.



Figure 5.8 shows the profile of wave propagation with a frequency in the region of double negativity. Noticeable difference to Figure 5.7 is the negative propagation direction of the wave phase with respect to positive energy flow. In the second and third windows, the phase direction is clearly seen pointing from right to left during the sequence of time evolution.

### 5.5.2 Wave packets

Group velocity is the velocity of the envelope of a wave group or packet. For a wave packet corresponding to a superposition of harmonic waves with a finite frequency band, the propagation behavior in a dispersive media like DN acoustic metamaterial should be of particular interest. One great advantage of considering the wave packet is that the frequency content of the packet can be controlled and the energy propagation direction can be easily identified as the propagation direction of the wave packet.

To this end, wave packets propagating in the metamaterial with double negativity are simulated in a similar fashion. Two wave packets in time as well as in frequency domain used for the simulation are illustrated in Figure 9. In Figure 9a, the wave packet possesses a frequency band approximately from  $\eta = \omega / \omega_0^{NMD} = 0.22$  to  $\eta = 0.47$  (in the double positivity region) with the central frequency at  $\eta = 0.346$ , while in Figure 9b, the wave packet possesses a frequency band approximately from  $\eta = \omega / \omega_{0,NMD} = 1.10$  to  $\eta = 2.10$  (in the double negativity region) with the central frequency at  $\eta = 1.559$ . Each packet is sent from the left end of the model. Same material properties are chosen so that the dispersion relation of the model is shown in Figure 5.6.

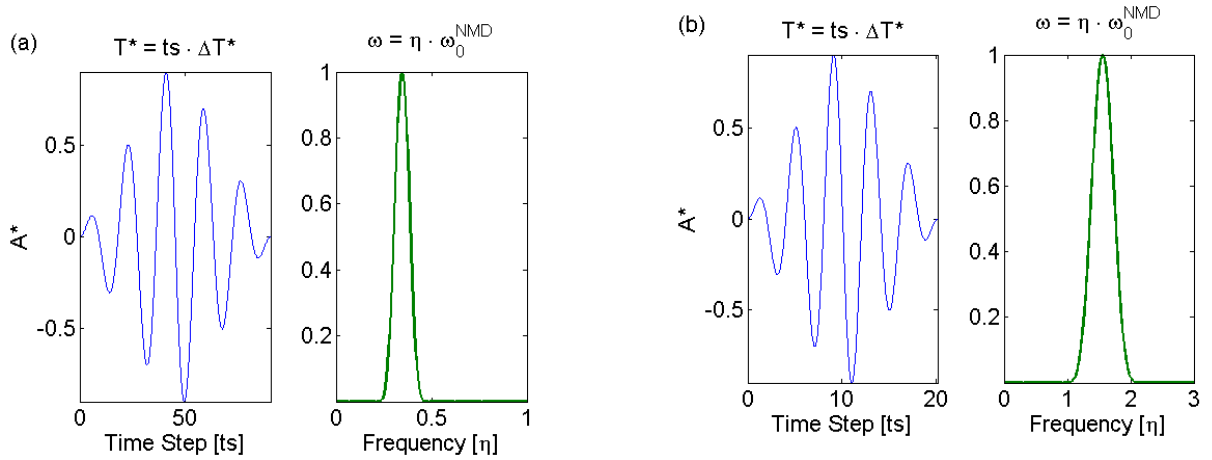


Figure 5.9 Two typical wave packets in time and frequency domain with (a) frequency band approximately from  $\eta = \omega / \omega_0^{NMD} = 0.22$  to  $\eta = 0.47$  (in the double positivity region) with the central frequency at  $\eta = 0.346$  and; (b) frequency band approximately from  $\eta = \omega / \omega_0^{NMD} = 1.10$  to  $\eta = 2.10$  (in the double negativity region) with the central frequency at  $\eta = 1.559$ .

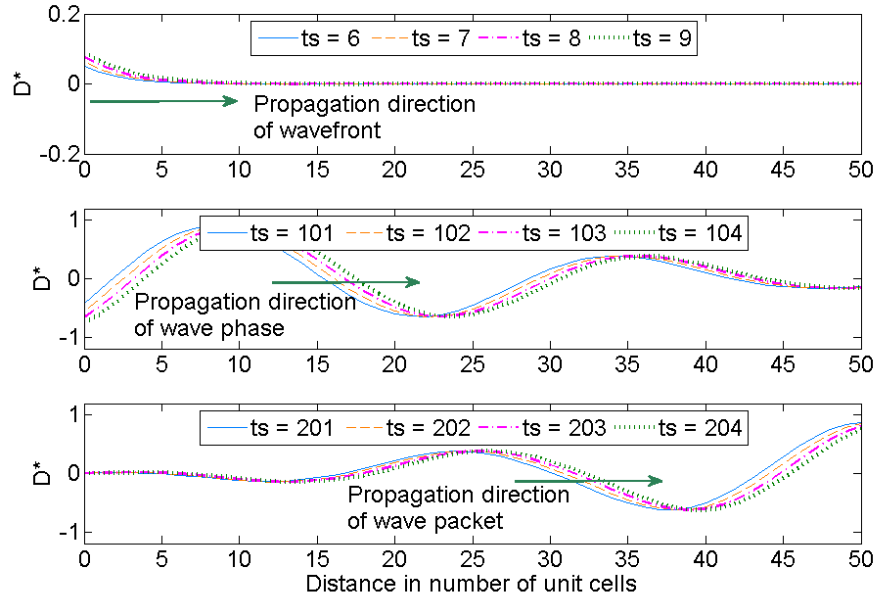


Figure 5.10 Snapshots of wave-packet propagation in finite DN model; Wave packet consists of frequency band approximately from  $\eta = \omega / \omega_0^{NMD} = 0.22$  to  $\eta = 0.47$  with the central frequency at  $\eta = 0.346$  and  $\omega_0^{NMD} = 115.47 \text{ rad/s}$  (in the double-positivity region;  $T^* = \omega_0^{NMD} \cdot t = ts \cdot \Delta T^*$  with  $\Delta T^* = 0.462$ ).

Figure 5.10 shows a few snapshots of wave propagation of the wave packet shown in Figure 5.9a, of which the central frequency is located at the positive effective mass density and positive effective elastic modulus region as shown in Figure 5.4. The wave packet propagates without much distortion since most of the spectral content travel with approximately the same speed, which is also evident in view of the dispersion curves shown in Figure 5.6. The energy flow direction is the moving direction of the wave packet, which is clearly from left to right. Note that a wave packet contains not just a single frequency, but a finite frequency band. It is therefore difficult to identify the phase velocity of from the propagation of the wave packet.

Next, consider the case when the frequency components of the wave packet are selected in the frequency region of double negativity. A wave packet of Figure 9b is generated for simulation. The frequency band of this wave packet is inside the double negativity region shown in Figure 5.4. The wave packet is sent from the left end and is clearly seen to propagate in the positive direction (left to right) from the top and bottom windows of Figure 5.11. Negative phase direction of the packet is expected and can be verified from the middle window of Figure 5.11.

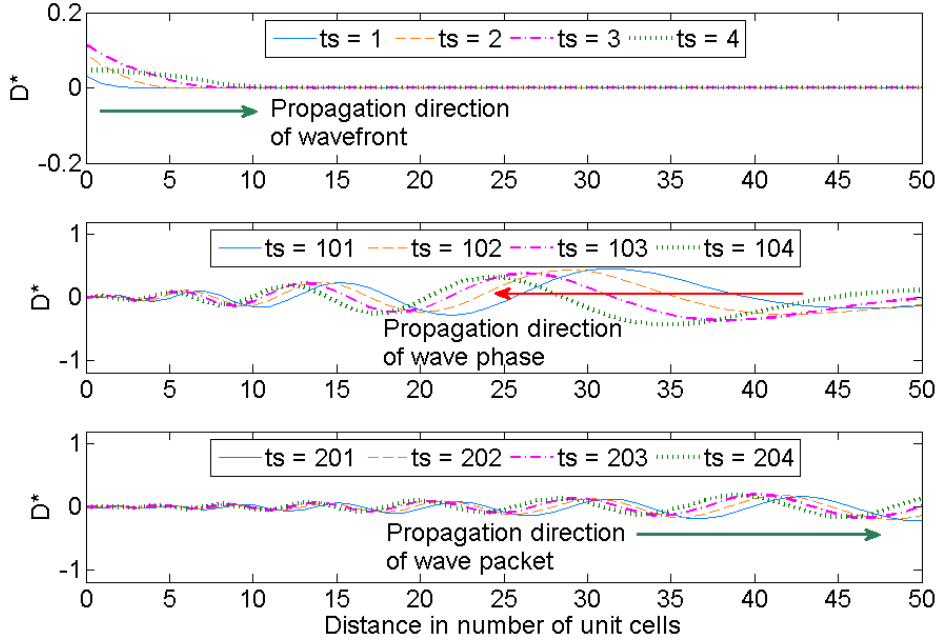


Figure 5.11 Snapshots of wave-packet propagation in the DN model Wave packet consists of frequency band approximately from  $\eta = \omega / \omega_0^{NMD} = 1.10$  to  $\eta = 2.10$  with the central frequency at  $\eta = 1.559$  and  $\omega_0^{NMD} = 115.47 \text{ rad} / s$  (in the double-negativity region;  $ts =$  time step;  $T^* = \omega_0^{NMD} \cdot t = ts \cdot \Delta T^*$  with  $\Delta T^* = 0.462$ ).

### 5.5.3 Discussion

The region of the dispersion curve with negative slope means a spectral range where the phase and group velocities are opposite in direction. Some researchers in the literature have termed the backward-wave phenomenon along with “negative group velocity” simply because, perhaps, in the  $\omega$ - $q$  diagram the slope of the dispersion curve is negative. For example, let us refer to the dispersion diagram in Figure 12 for illustration. The dispersion curves are reproduced from Figure 6, Case 2 in Section 5, for the DN model. Usually the first quadrant of the diagram is considered where  $\omega$  and  $q$  are both positive. For the first lowest propagation mode, both phase velocity and group velocity, according to the definition in Section 4, are positive. As for the second lowest propagation mode, in the first quadrant, the phase velocity is positive while the group velocity is negative.

The misleading and confusing conclusion of the “negative group velocity” may come from the fact that energy velocity is not directly provided by the dispersion curves in the first quadrant. In fact, the second branch of the dispersion curve should be plotted in the second quadrant where  $\omega$  is positive and  $q$  is negative. By so doing, the group velocity is positive while the phase velocity is, hence, negative.

## 5.6 Conclusion

We have proposed a one-dimensional mechanical model representing an acoustic metamaterial. The system can be modeled with an equivalent elastic solid which exhibits simultaneously negative effective mass density and effective Young's modulus in a certain frequency range. In this double negativity frequency range, harmonic waves propagate without attenuation. However, the phase velocity becomes opposite to the energy flow direction. In view of positive energy direction, it is the backward wave that propagates with negative phase velocity. Transient wave simulation results not only agree well with the analytical prediction, but also clearly illustrate the unusual wave phenomenon.

## 6. DESIGN AND ANALYSIS OF ANISOTROPIC ELASTIC METAMATERIALS

### 6.1 Introduction

An anisotropic elastic metamaterial made of heavy cylinder cores coated with elliptical soft layer and embedded in a matrix as shown in Fig. 1a is considered. The representative volume element (RVE) is identified and shown in Fig. 1(b). The microstructure is distributed in a rectangular lattice array. In the figure, the hard inclusion core is labeled as medium 1, the soft coating medium is labeled as medium 2, and the matrix is labeled as medium 3. The isotropic material constants of the inclusion core, the coating layer, and the matrix are  $\rho_1, E_1, \nu_1$ ;  $\rho_2, E_2, \nu_2$  and  $\rho_3, E_3, \nu_3$ , respectively. The radius of the core is  $a$ . The lattice constants along the  $X_2$  and  $X_3$  directions are denoted as  $d_2$  and  $d_3$ . The semimajor and semiminor axes of the ellipse are denoted as  $b_1$  and  $b_2$ , respectively. In the unit cell  $(k, l)$ , position of the center point is given in the global coordinate  $X_2 = X_2^l$  and  $X_3 = X_3^k$ . For convenience, we define a local polar coordinate system  $(r, \theta)$  as well as a local Cartesian coordinates  $(x_2, x_3)$  in the unit cell with  $x_2 = r \cos \theta$  and  $x_3 = r \sin \theta$ , as shown in Fig. 1(b). Strong anisotropic properties of the metamaterial along the  $X_2$  and  $X_3$  directions can be achieved by adjusting dimensions of the major and minor axes of the coating ellipse.

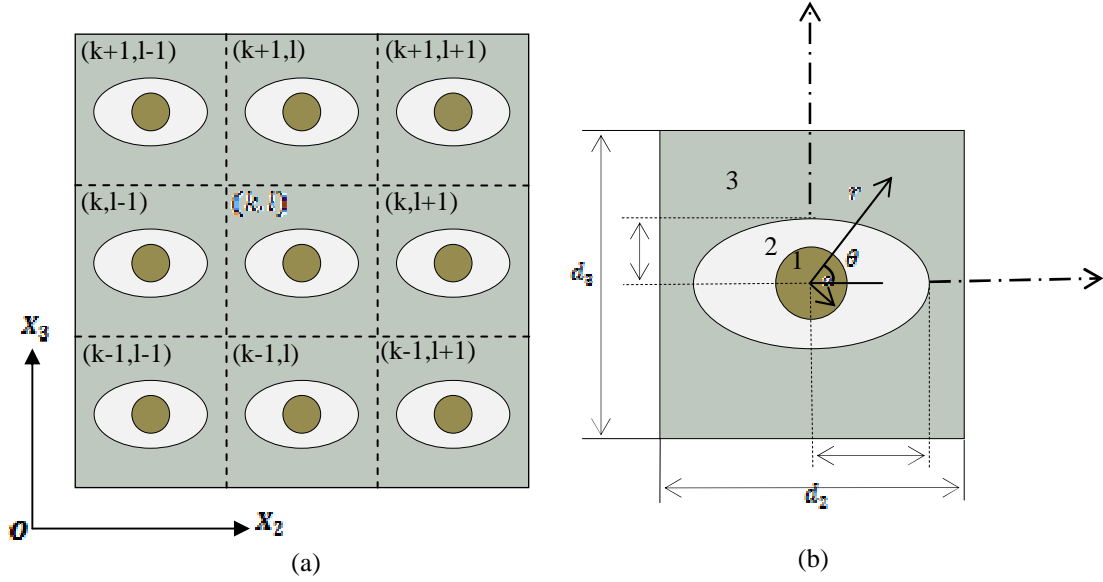


Fig. 6.1 (a) An anisotropic elastic metamaterial made of cylinders coated with elliptical soft layer in a matrix; (b) The  $(k,l)$  element (RVE).

Due to geometric complexity of the microstructure, analytical-based methods cannot be applied directly for the determination of the effective dynamic mass density [28]. In this study, a numerical-based method (FEM) will be adopted [8]. Consider the unit cell in Fig.6.1(b), time-harmonic displacements  $u_\alpha = \hat{u}_\alpha e^{i\omega t}$  with  $\alpha = 2,3$  are prescribed on the exterior boundary, and a harmonic analysis of the unit cell is performed by using the finite element method, from which resultant forces  $F_\alpha = \hat{F}_\alpha e^{i\omega t}$  on the exterior boundary can be obtained. The effective mass density tensor can then be numerically defined and determined by

$$\begin{Bmatrix} \hat{F}_2 \\ \hat{F}_3 \end{Bmatrix} = -\omega^2 A_c \begin{bmatrix} \rho_{22}^{eff} & \rho_{23}^{eff} \\ \rho_{32}^{eff} & \rho_{33}^{eff} \end{bmatrix} \begin{Bmatrix} \hat{u}_2 \\ \hat{u}_3 \end{Bmatrix} \quad (6.1)$$

where  $A_c = d_2 d_3$  is the area of the unit cell. To demonstrate that the mass density follows the coordinate transformation law, effective mass density tensor in an arbitrary coordinate system  $(x,y)$ , as shown in Fig.2, is similarly determined. In the figure,  $(x_2, x_3)$  is a rectangular Cartesian coordinate system in principal directions and  $(x,y)$  is an arbitrary Cartesian coordinate system. It should be mentioned that the unit cell in Fig. 2 is specifically suggested for simplification of numerical calculation, in which the outer matrix seems to follow the unit cell transformation. This is because the outer host matrix is mainly functioned as an effective mass in the calculation of the effective mass density of the unit cell. Therefore, determination of the effective mass density is independent on the outer matrix geometry. Based on the numerical results of the unit cell, it can be proved that the effective mass density follows the coordinate transformation law as

$$\begin{bmatrix} \rho_{xx}^{eff} & \rho_{xy}^{eff} \\ \rho_{yx}^{eff} & \rho_{yy}^{eff} \end{bmatrix} = \begin{bmatrix} C^2 \rho_{22}^{eff} + S^2 \rho_{33}^{eff} & CS(\rho_{33}^{eff} - \rho_{22}^{eff}) \\ CS(\rho_{33}^{eff} - \rho_{22}^{eff}) & C^2 \rho_{33}^{eff} + S^2 \rho_{22}^{eff} \end{bmatrix} \quad (6.2)$$

where  $C = \cos\delta$ ,  $S = \sin\delta$ , and  $\delta$  is the angle of the transformation. Therefore, the effective mass density admits the second-order tensorial property.

**Table 6.1** The microstructure geometrical parameters.

Lattice parameters	Elliptical coat	Circle coat
$d_2 = d_3$	20mm	20mm
$a$	3mm	5.155mm
$b_1$	7mm	7.14mm
$b_2$	5mm	7.14mm

**Table 6.2** The constituent material parameters.

The parameters	Core: lead	Coating: rubber	Matrix: epoxy
Mass density	$\rho_1: 11.31 \times 10^3 \text{ kg/m}^3$	$\rho_2: 0.92 \times 10^3 \text{ kg/m}^3$	$\rho_3: 1.11 \times 10^3 \text{ kg/m}^3$
Young's modulus	$E_1: 1.3 \times 10^{10} \text{ N/m}^2$	$E_2: 1.5 \times 10^6 \text{ N/m}^2$	$E_3: 2.35 \times 10^9 \text{ N/m}^2$
Poisson's ratio	$\nu_1: 0.435$	$\nu_2: 0.499$	$\nu_3: 0.38$
Area	$A_1: \pi a^2$	$A_2: \pi(b_1 b_2 - a^2)$	$A_3: d_2 d_3 - \pi b_1 b_2$

Fig. 6.1 shows the effective mass density of the elastic metamaterial along a direction  $\delta = 30^\circ$  by using the FEM model, where  $\rho_{ave} = (\rho_1 A_1 + \rho_2 A_2 + \rho_3 A_3)/A_c$  is the average static mass density for the composite. The microstructure geometry parameters and the constituent material parameters are given in Tables 6.1 and 6.2, respectively. From the figure, we can clearly see that the effective mass density is frequency-dependent, anisotropic ( $\rho_{xx}^{eff} \neq \rho_{yy}^{eff}, \rho_{xx}^{eff} \neq 0$ ) and becomes negative around the resonant frequency. For the metamaterial with the current microstructure, two different resonant frequencies along  $x_1$  and  $x_2$  directions can be found as  $f^{*1} = 862\text{Hz}$  and  $f^{*2} = 950\text{Hz}$ , respectively, which indicate anisotropy of the metamaterial. The significant difference between  $\rho_{xx}^{eff}$  and  $\rho_{yy}^{eff}$  can be observed when the frequency is close to the resonant frequency. It is also interesting to note that the mass density become isotropic ( $\rho_{xx}^{eff} = \rho_{yy}^{eff}, \rho_{xx}^{eff} = 0$ ) when the frequency is much less or much larger than the resonant frequency.

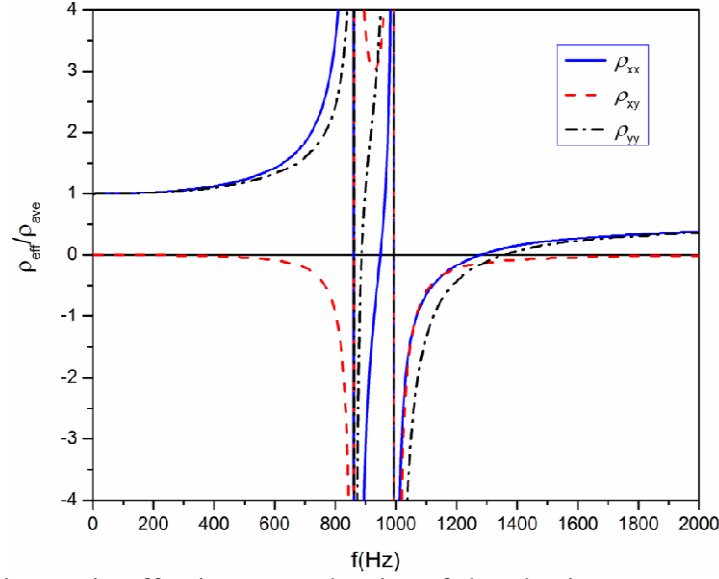


Fig. 6.1. The anisotropic effective mass density of the elastic matatmaterial predicted by the FEM model along a direction  $\delta = 30^\circ$ .

## 6.2 Fabrication and Testing of Anisotropic Elastic Metamaterial

The proposed anisotropic metamaterial plates were manufactured with  $\delta=0$  and  $\delta=90$ , respectively. The elliptic holes were first cut in an aluminum (Al) plate (Type 6061) with 600mm in length, 33mm in width and 3.175mm in thickness using a computer numerical control (CNC) machine. The major and minor axes of the elliptic hole are 9.9mm and 7.1mm, respectively. The periodic holes (3X10) are arranged in a rectangular lattice with lattice constant 11 mm. Then, pure lead rods ( $\Phi=3.175\text{mm}$ , *ESPI Metals*) and epoxy ( $\rho = 1033\text{kg/m}^3$ ,  $E = 0.595\text{GPa}$ ,  $\nu = 0.37$ , Crystal Clear<sup>®</sup> 202, *Smooth-On Inc.*) were filled in the elliptic holes to form the anisotropic metamaterial plate, as shown in

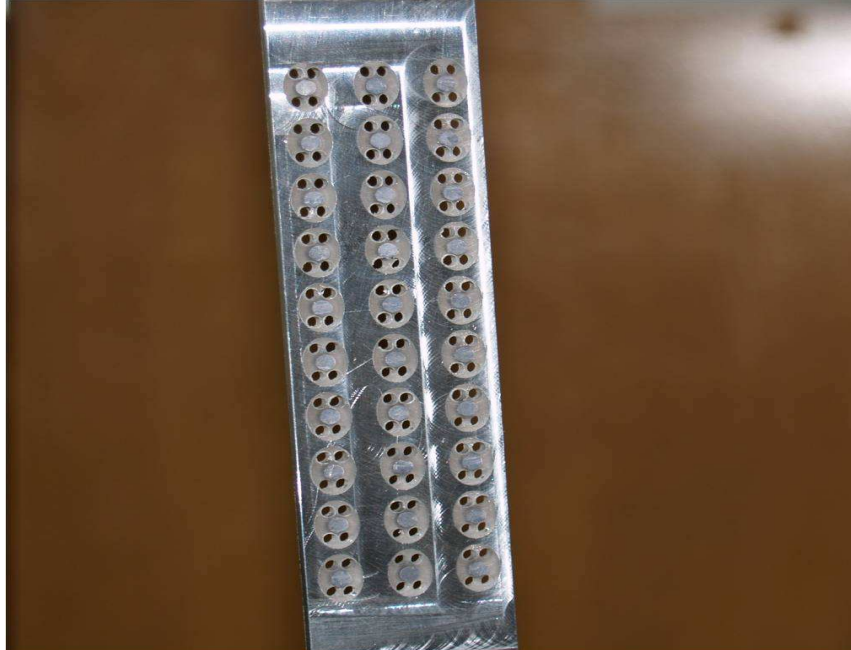


Fig. 6.2 A fabricated anisotropic metamaterial plate



Fig. 6.2. The center positions of lead rods are controlled through the help of the additional plate with exact location holes. To increase anisotropy of the metamaterial, four small circular holes are drilled in the epoxy.

### 6.2.1 Anisotropic band-gap validation

To investigate the band-gap behavior of the metamaterial, the transmission property of the longitudinal wave propagating along the  $x_2$  direction is first studied experimentally. The set-up of the transmission experiment is shown in Fig. 6.3. Two rectangular piezoelectric disks, functioned as a pair of actuators, are surface-bonded to the up and down surfaces of the plate in order to generate longitudinal wave. Two circular piezoelectric disks, functioned as a pair of sensors, are used to receive the transmitted signals after the metamaterial. By using two symmetric sensors on the plate, the out-of-plane components can be eliminated and the ratio of signal-to-noise can be significantly increased for the in-plane component. Fig. 6.4a shows the experimental measurement of the transmission properties of the metamaterial at  $\delta=0$ . For validation, the exact numerical simulation results are also plotted in the figure. From the figure, the band-gap of the metamaterial can be found in the region of frequency (17.2kHz, 21.6kHz). It should be mentioned that the ‘small gap’ around 12.8kHz from the numerical simulation is because the sensor’s position is located at the node of the standing wave, which is caused by the band-gap behavior. Fig. 6.4b shows the experimental measurement of the transmission properties of the metamaterial at  $\delta=90^\circ$ . As expected, the band-gap of the metamaterial at  $\delta=90^\circ$  is different from the metamaterial at  $\delta=0$  the band-gap frequency is in the frequency regime (23.8kHz, 31.6kHz). However, the experimental results can accurately capture the band-gap behavior of the metamaterial.

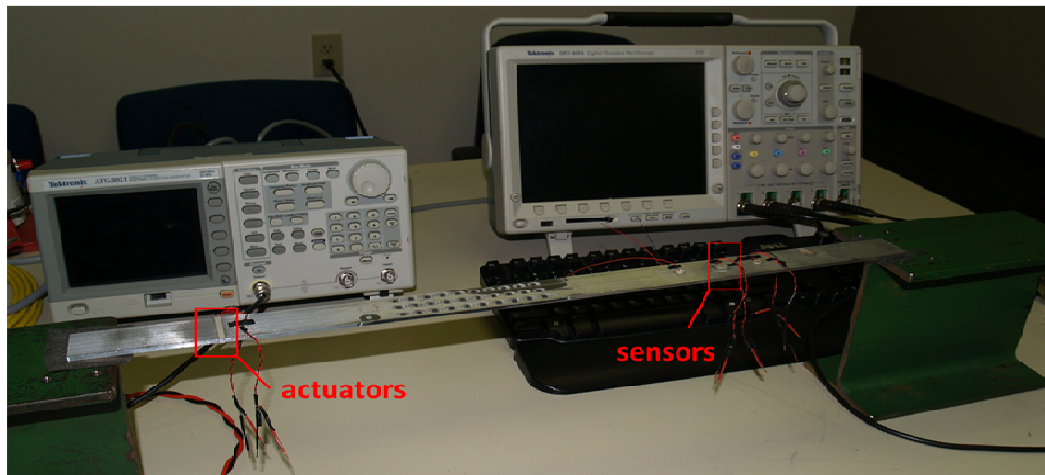
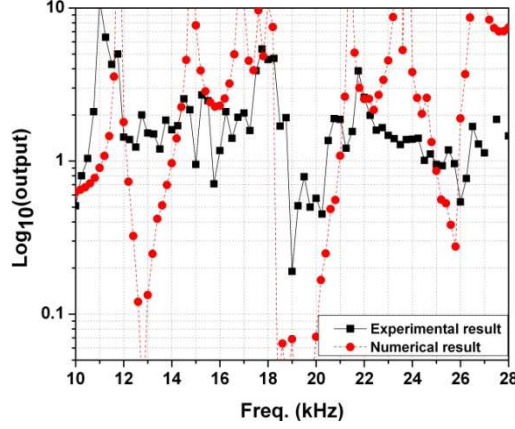
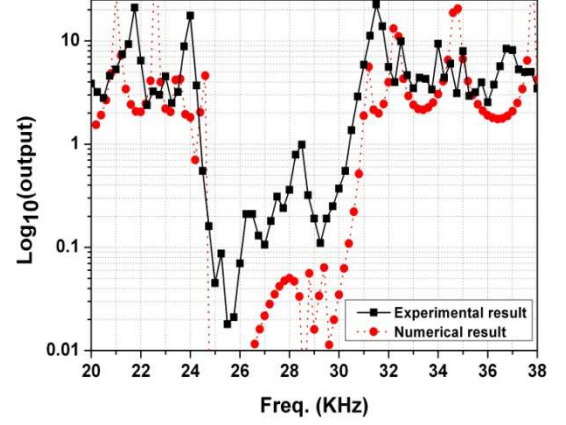


Fig. 6.3 Experimental set-up of transmission testing of the metamaterial





(a)

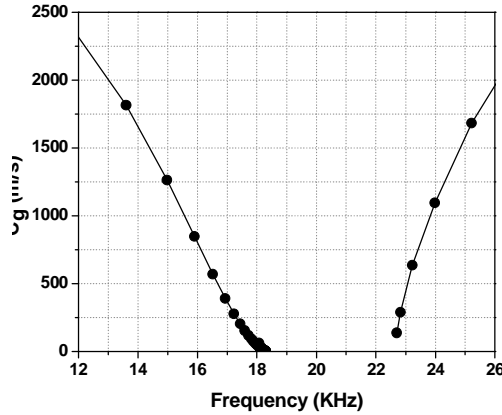


(b)

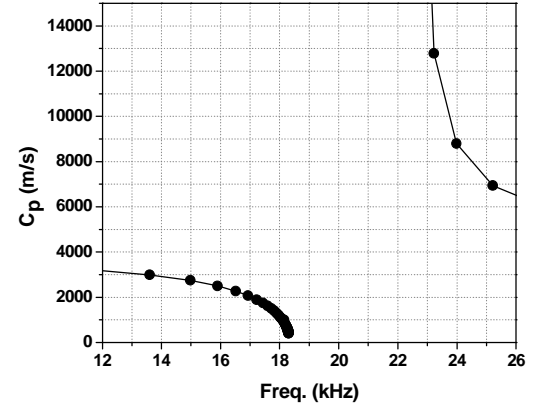
Fig. 6.4 Experimental transmission measurements of longitudinal wave in the anisotropic metamaterial plates for  $\delta=0$  (a) and  $\delta=90$  (b)

### 6.2.2 Determination of group and phase velocities of the metamaterial

Analytically, the group velocity and phase velocity of the longitudinal wave propagating along the  $x_2$  direction in the metamaterial plate with  $\delta=0$  can be easily obtained from the dispersion relation. Based on  $c_g = \frac{d\omega}{dk}$ , the group velocity can be obtained in a function of frequency by applying central difference to lowest two longitudinal branches of the dispersion relation as shown in Fig. 6.5(a). The phase velocity can be obtained from  $c_p = \frac{\omega}{k}$ , as shown in Fig. 6.5 (b).



(a)



(b)

Fig. 6.5 Group velocity (a) and phase velocity (b) of the metamaterial with  $\delta=0$  obtained from the lowest two longitudinal branches of the dispersion relation.

In order to experimentally measure the group and phase velocity of longitudinal wave propagation in the anisotropic metamaterial plate, a transient experimental set up is proposed in Fig. 6.6, which is similar to the set-up of the harmonic testing. The two rectangular piezoelectric patches, functioned as actuators, are used to generate in-plane longitudinal wave. Unlike the transmission study, two pairs of symmetric bonded piezoelectric sensors are used to collect the in-plane wave signals. Sensor pair 1 is before the metamaterial area and the sensor pair 2 is after the metamaterial area as shown in Fig. 6.6. In order to capture the complete wave propagation in the anisotropic metamaterial plate without the interference of the reflected waves, the total length of the anisotropic metamaterial plate is extended to 2.5m by welding two Al plates with the same width to the two ends of the metamaterial plate.

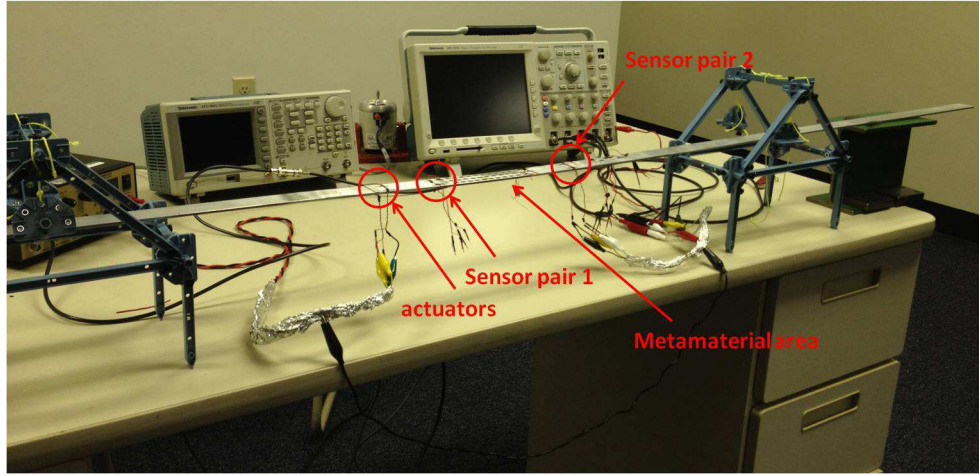


Fig. 6.6 Experimental set up for group velocity and phase velocity measurement of the metamaterial

A broadband wave signal  $V(t) = A[1 - \cos(2\pi ft)]\sin(2\pi ft)$  is chosen, where  $A$  is the amplitude and  $f$  is the frequency. Input signals with  $f=13.5\text{kHz}$ ,  $15.5\text{kHz}$  and  $24.5\text{kHz}$  are used in the experiment in the order to cover the interested frequency range in Fig. 6.5. The continuous wavelet transform (CWT) based on the Gabor wavelets, which has been demonstrated to be very useful as a time-frequency analysis tool of wave signals in structural health monitoring (SHM), is used to obtain the group and phase velocity dispersion curves. The continuous wavelet transform (CWT) of a given signal  $s(t)$  is given by:

$$WT(a, b) = \frac{1}{\sqrt{a}} \int_{-\infty}^{+\infty} s(t) \overline{\psi\left(\frac{t-b}{a}\right)} dt \quad (6.3)$$

where  $\psi(t)$  is called the mother wavelet function and the overline indicates the complex conjugate.  $a$  and  $b$  are known as the scale and translation parameters, respectively. The reciprocal of  $a$  is associated with frequency and  $b$  is related to time. Gabor function is chosen as the mother wavelet function in our analysis since it can provide a better resolution both in the time and frequency domain than any other wavelets based on Heisenberg Uncertainty.

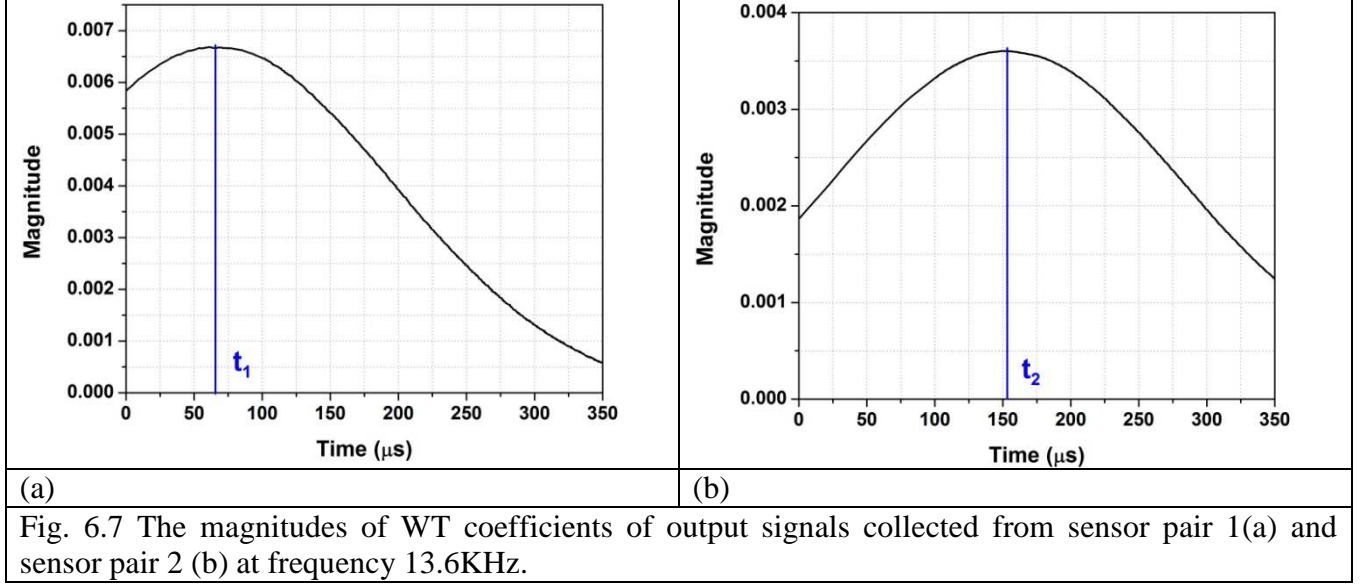


Fig. 6.7 shows the magnitudes of WT coefficients of the measured output signals collected from sensor pair 1 and sensor pair 2 at a given scale  $\alpha$ , which is related with certain frequency  $f$ . The arrival times for the output signals in two sensor pairs are determined by the peak locations in Fig. 6.7 (a) and (b), respectively. The time difference,  $\Delta t$ , is then calculated. Since the distance between sensor pair 1 and sensor pair 2 is  $d = 215mm$  and the length of the metamaterial area is  $d_0 = 110mm$ , the group velocity as a function of frequency can then easily determined as:

$$c_g(f) = \frac{d_0}{[\Delta t(f) - \frac{d-d_0}{c_g^M}]} \quad (6.4)$$

where  $c_g^M$  is the group velocity of the matrix material,  $c_g^M = 5400m/s$  is used for the aluminum plate at low frequencies.

Figure 6.8 shows the experimental measured group velocity of the metamaterial with  $\delta=0$ . For the comparison, analytical solution obtained from the dispersion relation of the metamaterial in Fig. 6.5 is added for the reference. Good agreements between the theoretical result and the experimental measurement can be found in the most interested frequency regime.

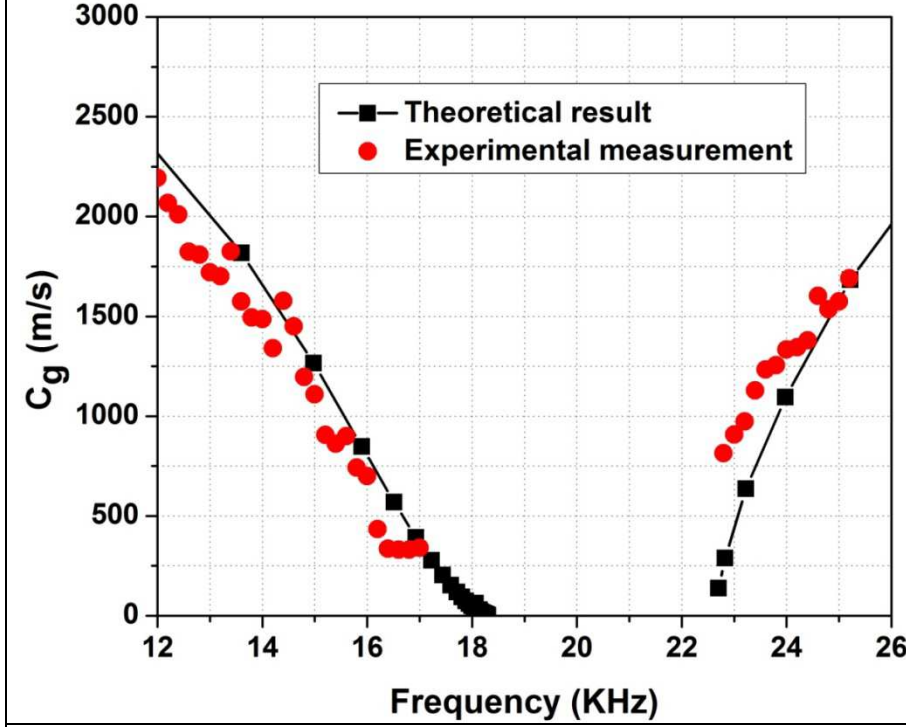


Fig. 6.8 Comparison of the group velocity from the numerical simulation and experimental testing.

In order to calculate the phase velocity, the phase angle,  $\phi(a, b)$ , of the WT coefficient needs to be considered. At a given scale  $a$ , the corresponding phase angle for the output signal at arrival time in each sensor pair is determined and the phase difference  $\Delta\phi$  between the received signals in sensor pair 1 and sensor pair 2 can be calculated. Then, the phase velocity is obtained in a function of frequency using the following relation:

$$C_p(f) = \frac{d_0}{(\Delta t(f) + \frac{\Delta\phi(f)}{2\pi f} - \frac{d - d_0}{C_p^M})}$$

where  $\Delta t$  is the arrival time difference and  $C_p^M$  is the phase velocity of the matrix material. Fig. 6.9 shows the comparison of the phase velocity from the experimental testing and the theoretical result from the dispersion relation of the metamaterial. Similarly, good agreements can be observed to show the feasibility of the proposed experimental approach for determination of the group and phase velocities of the elastic metamaterial.

Finally, the effective dynamic mass density of the anisotropic metamaterial can be estimated by the experimentally obtained phase velocity and the effective stiffness matrix. The effective stiffness of the metamaterial can be directly determined through the unit cell analysis and is found that it is not dependent on the wave frequency. Using the equation  $\rho_x^{eff}(f) = C_{xx}^{eff} / (C_p)^2$ , the effective dynamic mass density of the anisotropic metamaterial along x direction can be experimental determined as shown in Fig. 6.10. The very good agreement with the numerical solution can be also observed.

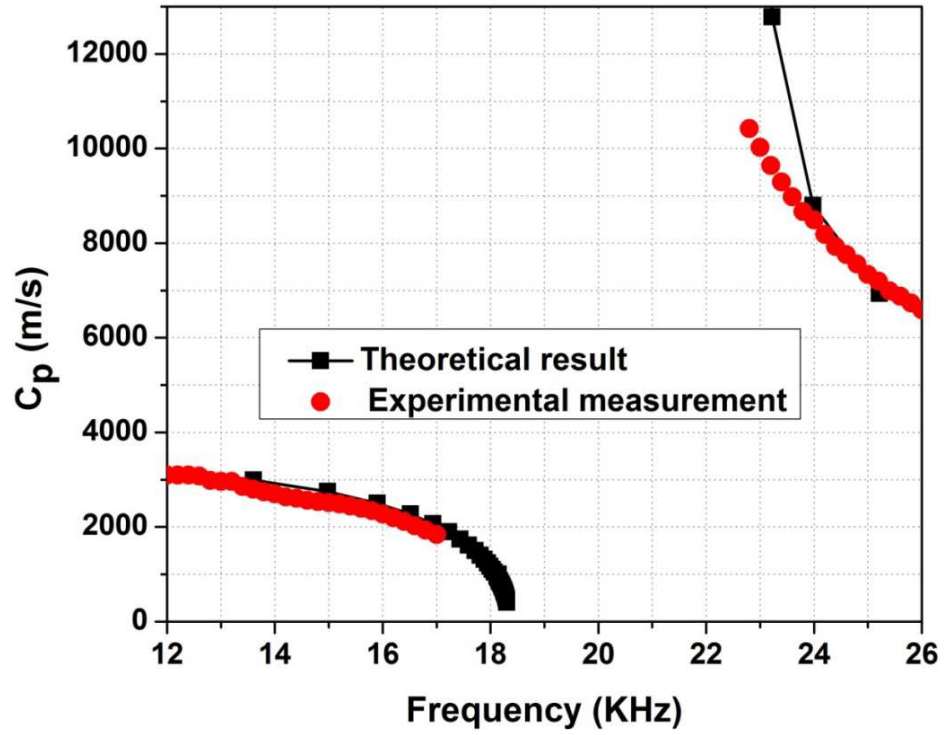


Fig. 6.9 Comparison of the phase velocity from the numerical simulation and experimental testing

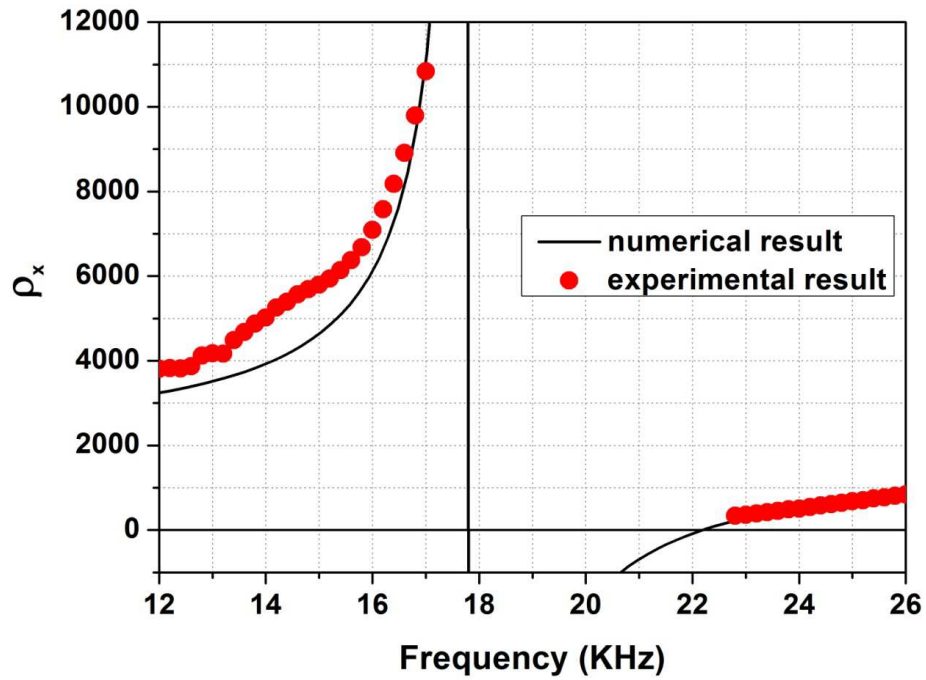


Fig. 6.10 Comparison of the mass density along x2 direction of the metamaterial from the numerical simulation and experimental testing

## 7. DESIGN OF BROADBAND ELASTIC METAMATERIALS

### 7.1 Introduction

Although many metamaterials have been proposed, narrow working frequencies of metamaterials have limited their applications (Li et al., 2009; Capolino, 2009; Cui et al., 2010). In view of this, there are several papers which proposed to solve the narrow band gap problem. However, most of them focused on optical metamaterials; there are just a few literatures developing acoustic/elastic broadband metamaterials. Zigoneanu et al. (2011) used strong anisotropic acoustic metamaterials to broaden band gap up to 500–3000 Hz. Meng et al. (2012) applied genetic algorithm to achieve the optimized broadband sound absorption 800–2500 Hz. In this study, we focus on the design of microstructures to improve the bandwidth up to 3370 Hz starting with a band-gap lower bound of 292 Hz. Three metamaterial models with single negativity are proposed, and parametric studies as well as comparisons are made to obtain metamaterials with large band gaps. Moreover, the start frequency of the band gap is in hundreds of Hertz.

### 7.2 Three Models for Single Negative (SN) Metamaterials

Three microstructures with dimensions are designed for metamaterials as shown in Figs. 7.1 – 7.3. The material properties of these three models are listed in Tables 7.1 – 7.3, respectively. The three types of metamaterials were fabricated with a 3D printer using a polymer ink. Figs 7.4 and 7.5 show a strip of the Type 2 and Type 3 metamaterials, respectively. The thickness of these metamaterials varies over the microstructure in order to achieve the equivalent material properties listed in the tables.

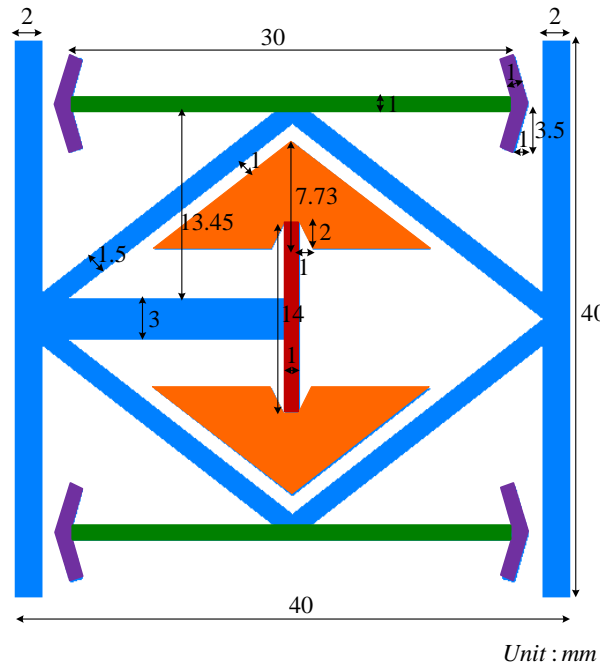


Fig. 7.1 Type 1 SN metamaterial model



TABLE 7.1 Material parameters for the Type 1 SN microstructure

Marked area	Mass density $\rho$ <i>kg / m<sup>3</sup></i>	Young's modulus $E$ <i>GPa</i>	Poisson's ratio $\nu$
Blue	1300	5.0000	0.49
Purple	4000	15.3846	0.49
Green	1615	6.2115	0.49
Orange	4000	15.3846	0.49
Red	1690	6.5000	0.49

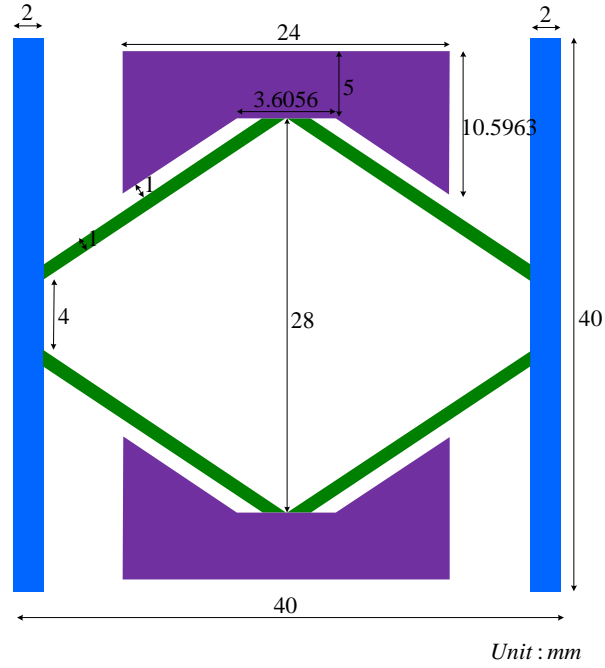


Fig. 7.2 Type 2 SN metamaterial model

TABLE 7.2 Material parameters for the Type 2 SN microstructure

Marked area	Mass density $\rho$ <i>kg / m<sup>3</sup></i>	Young's modulus $E$ <i>GPa</i>	Poisson's ratio $\nu$
Blue	1300	5.0000	0.49
Purple	2000	7.6923	0.49
Green	1500	5.7692	0.49

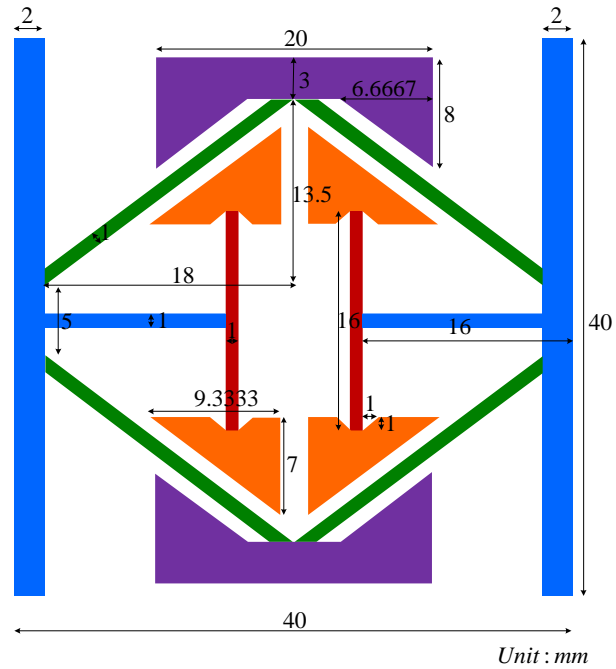


Fig. 7.3 Type 3 SN metamaterial model

TABLE 7.3 Material parameters for the Type 3 SN microstructure

Marked area	Mass density $\rho$ $kg / m^3$	Young's modulus $E$ $GPa$	Poisson's ratio $\nu$
Blue	1300	5.0000	0.49
Purple	2000	7.6923	0.49
Green	1500	5.7692	0.49
Orange	5200	20.0000	0.49
Red	5200	20.0000	0.49



Fig. 7.4 Type 2 SN metamaterial manufactured by a 3D printer



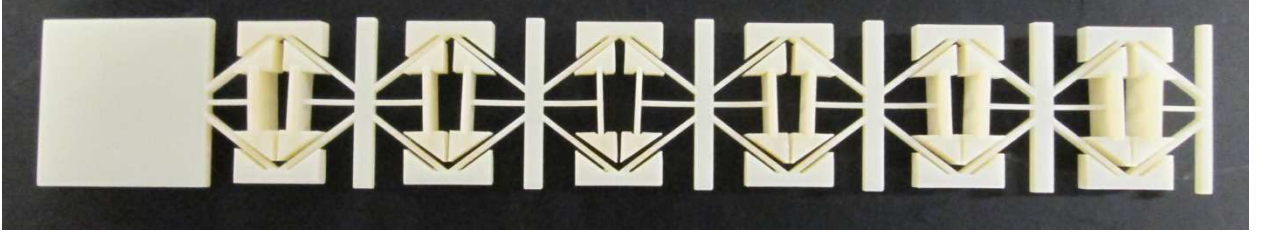


Fig. 7.5 Type 3 SN metamaterial manufactured by a 3D printer

In the Type 1 SN metamaterial model shown in Fig. 7.1., the two green horizontal beams with length of 30 mm and width of 1 mm serve as two vertical springs with the desired frequency to form negative Young's modulus (NYM) resonator. Because the rhombus frame is only used for transmitting force, the width of frame is designed as 1.5 mm to avoid the eigenmode coupling between horizontal beam bending and frame stretching. In addition, a red vertical beam serving as two horizontal springs and supporting triangular-shapes masses is used as negative mass density (NMD) resonator. The material properties are chosen to broaden the bandwidth by combining bandgaps of NYM and NMD.

Instead of using beam bending, Type 2 SN metamaterial uses frame stretching as the stiffness of the resonator. As shown in Fig. 7.2, the rhombus frames serve as two vertical springs supporting purple masses to achieve NYM local resonance. It is noted that Type 2 SN model is only with NYM. The geometry and material parameters are chosen from a parametric study and listed in Table II.

Type 3 SN metamaterial is formed by adding two resonators to Type 2 SN model. As shown in Fig. 7.3, the two red vertical beams serve as two sets of horizontal springs and support orange masses to achieve NMD local resonance when they move in phase. In addition, the frame stretching resonator and the symmetrical mode of the internal masses (when the two red vertical beams move  $180^\circ$  out-of-phase) form two sets of NYM resonators with desired frequencies. The band-gap region is broadened by combining multiple NMD and NYM bandgaps.

### 7.3 Mode Shapes and Dispersion Curves

Considering one-dimensional longitudinal harmonic wave propagation, the displacement can be expressed as

$$u(x,t) = Ae^{iq(x-ct)} = Ae^{iqx}e^{-i\omega t} \quad (7.1)$$

where  $c$  denotes phase velocity and  $q$  wave number. By selecting two locations as nodes (zero displacement), Eq. (7.1) can be treated as a free vibration problem of a finite body with the fixed end condition. With this concept, we constrain the horizontal movements of the left and right ends of a 100-unit-cell long strip (so the two ends become nodal points) for modeling the infinite number of unit cells metamaterial with 100 unit cell periodicity. The result of the free vibration analysis yields the natural frequencies and the corresponding mode shapes, from which wave numbers are obtained.

The ABAQUS commercial software is used for the finite element analysis. Since the beam bending serves as the stiffness of resonator, accuracy for beam bending estimation is crucial. For element type selection, the incompatible mode element (CPS4I) is applied due to its efficiency for bending calculation. Four CPS4I elements are placed along the thickness of the beam to achieve element-number-convergence.

Figs 7.6–7.8 show the dispersion curves for Types 1–3 SN metamaterials. Each passing band corresponds to a distinct RVE vibration mode, as listed in Table 7.4 and Table 7.5.

Dispersion curves for the Type 1 SN microstructure are shown in Fig. 7.6, the NMD and NYM resonators are optimized by minimizing the passing band between two adjacent bandgaps (the narrow passing band is 509.96–510.17 Hz). It is noted that the other narrow passing band with frequencies 463.35–463.47 Hz in Fig. 7.6 is caused by the rotational mode of the horizontal beams. If the two narrow passing bands are neglected, the overall band gap region is 403–554 Hz, firstly caused by NMD then by NYM. The two local resonances in Type 1 SN metamaterial are both produced by beam bending.

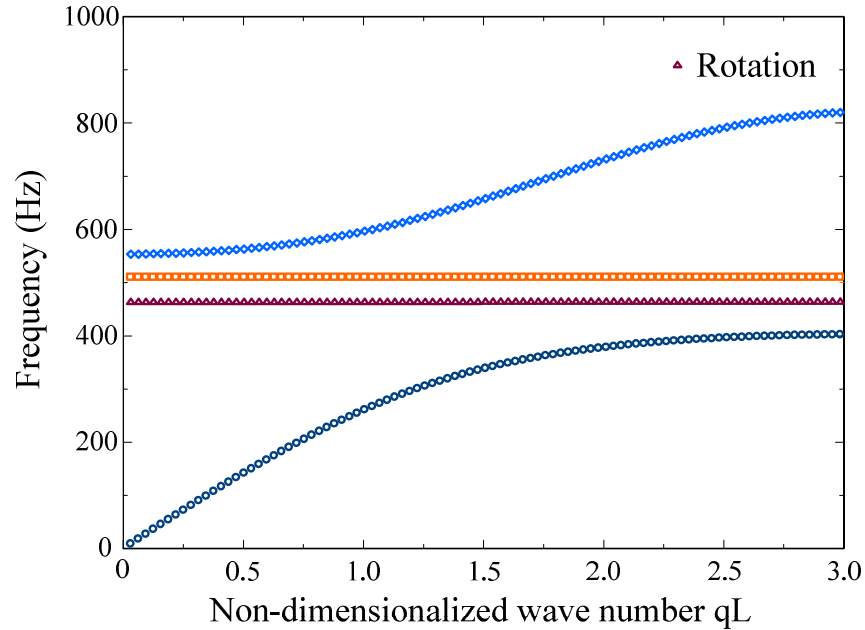


FIG. 7.6 Dispersion curves for the Type 1 SN model

Fig. 7.7 shows the dispersion curves for Type 2 SN metamaterial. If the narrow passing band from the rotational mode (505.41–506.90 Hz) is ignored, the bandgap region is 345–3097 Hz. This bandgap is caused by frame stretching which produces a much broader bandgap than the beam bending mode.

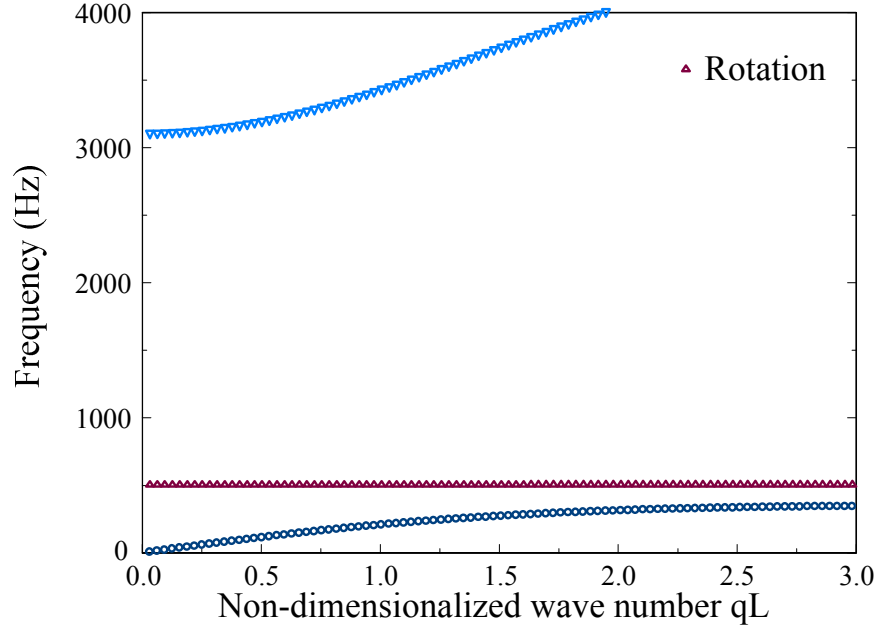


FIG. 7.7 Dispersion Curves for the Type 2 SN model

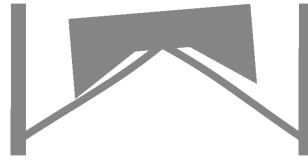
TABLE 7.4 Mode shape of the Type 2 SN model

Frame stretching mode



340.85 Hz

Rotational mode



501.93 Hz

The dispersion curves for Type 3 SN metamaterial are shown in Fig. 7.8. There are two narrow passing bands within the total bandgap region of 292–3694 Hz. They are a rotational mode with frequencies 752.40–755.24 Hz, and a double negativity region with frequencies 1064.8–1097.3 Hz. The overall bandgap region is caused by the frame stretching mode (NYM), the symmetrical mode of internal masses (NYM), and the anti-symmetrical mode of internal masses (NMD). The resonators are designed in order to form a large combining band-gap region. It is noted that the Type 3 SN model broadens the bandgap region of the Type 2 SN model by adding two extra resonators.

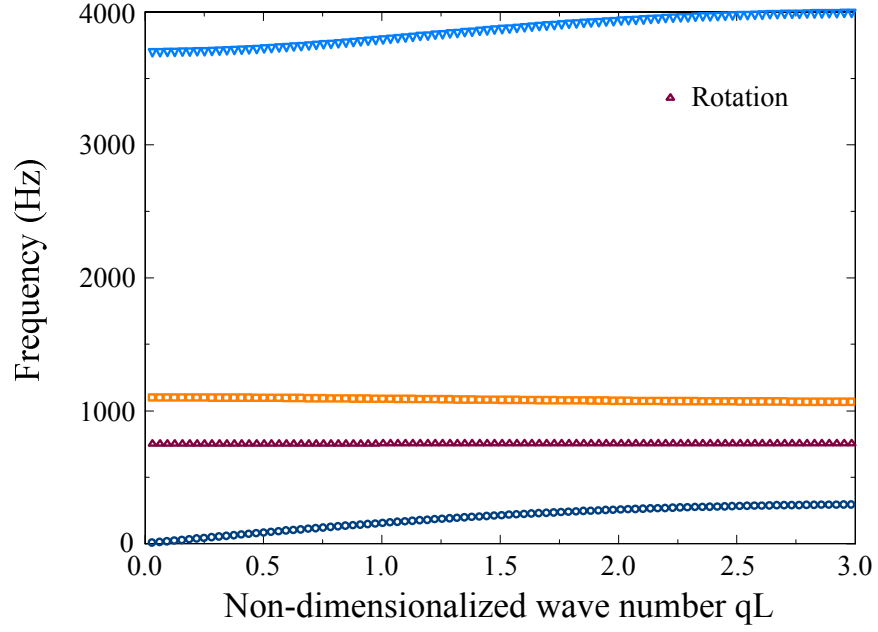






FIG. 8. Dispersion curve for the Type 3 SN model

TABLE 7.5 Mode shape of the Type 3 SN model

Frame stretching mode	Rotational mode
	
287.05 Hz	746.23 Hz
Internal masses symmetrical mode	Internal masses anti-symmetrical mode
	
1062.0 Hz	1089.8 Hz

#### 7.4 Representative Volume Element Steady State Analysis

In addition to utilizing dispersion curves to obtain the bandgap region, we also investigate the use of the representative volume element (RVE) steady-state analysis. Taking Type 3 SN model for example, for long wave motions, the frequency-dependent effective modulus of the metamaterial can be obtained by applying symmetrical loading  $F_0 \sin \omega t$  on the RVE as shown in Fig. 7.9(a). The displacements at side edges of the

RVE are constrained straight and with the corresponding displacements  $u = \pm u_0 \sin \omega t$ . The dynamic stiffness of the RVE is hence given by

$$k = \frac{F_0}{2u_0} \quad (7.2)$$

It is noted that the stiffness of the unit cell defined by Eq. (7.2) is proportional to the effective Young's modulus of the metamaterial.

The dynamic stiffness frequency spectrum is shown in Fig. 7.9(b). The bandgap region is defined as the frequency range within which  $k$  has negative value, i.e., 294–866 Hz and 1064–3694 Hz.

The effective mass density of the microstructures can be obtained from the dynamic response of the RVE loaded as in Fig. 7.10(a). The displacements at side edges of the RVE are set to be equal and straight. The effective mass of the unit cell is presented by

$$m_{eff} = -\frac{F_0}{u_0 \omega^2} \quad (7.3)$$

The effective mass frequency spectrum is shown in Fig. 7.10(b). The bandgap region is defined as the frequency range where  $m_{eff}$  becomes negative, i.e., 867–1099 Hz. It is noted that the small peak in Fig. 7.10(b) at frequency 755 Hz is caused by the rotational mode, which can also be observed in dispersion curve as shown in Fig. 7.8.

The bandgaps predicted using RVE are listed in Tables VI – VII together with the bandgaps obtained from the dispersion curves using 100 unit cells based on free vibration analysis. It is evident that the RVE steady-state analysis is very accurate in estimating the bandgaps. One shall also notice that the frequency range 1065–1097 in Table VII of the dispersion curve approach is the double negativity region (band-gap overlap from NMD and NYM).

The reason for RVE precisely determining band-gap region lies in the accurate estimation for dispersion curve in longest and shortest waves. When the wave length is much larger than the characteristic length of RVE, the boundary condition for each unit cell for dispersion curve coincides with the assumption we put on RVE: the side edges of RVE have equal displacement magnitude. For shortest wave length in each branch of dispersion curve, the half wave length is exactly the same as the characteristic length of one unit cell. As a result, each unit cell in dispersion curve has the equal displacement magnitude on its edge, which is also the same as the boundary condition we use for RVE analysis. It shall be pointed out that the method for RVE steady-state simulation has limitation in predicting the band-gap region for vibration mode involving non-straight side edges in unit cells.

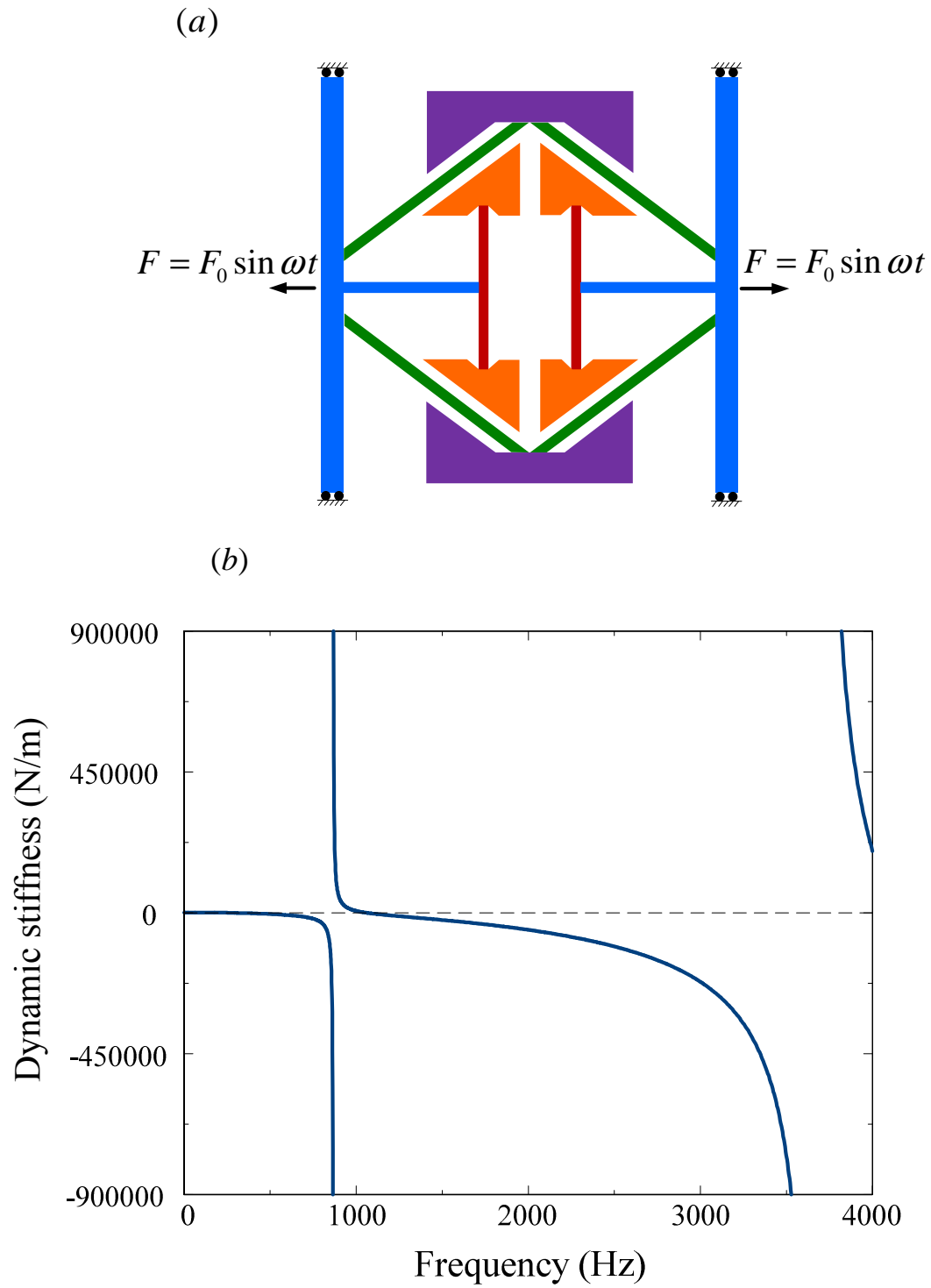


FIG. 7.9. (a) Testing dynamic stiffness (effective Young's modulus). (b) Dynamic stiffness frequency spectrum.

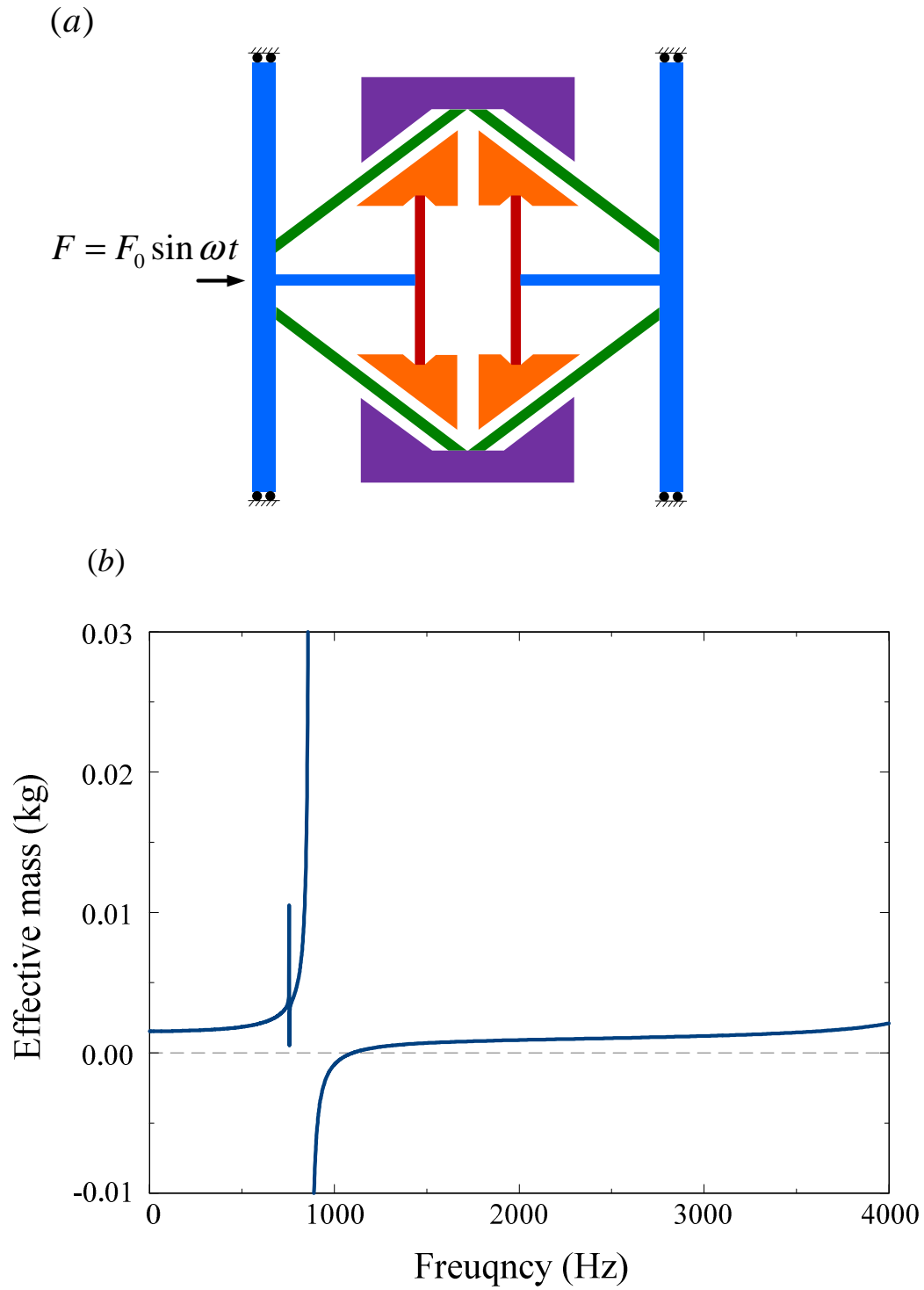


Fig. 7.10. (a) Testing effective mass density. (b) Effective mass frequency spectrum.

TABLE 7.6 Comparison of band gap region prediction for Type 2 SN model	
Method	Bandgap Region Estimation (Hz)
Dispersion Curve	345 – 3097
RVE steady-state analysis	347 – 3097

TABLE 7.7. Comparison of band gap region prediction for Type 3 SN model

Method	Bandgap Region Estimation (Hz)
Dispersion Curve	292 – 1065
	1097 – 3694
RVE steady-state analysis	294 – 866 (From RVE NYM test)
	867 – 1099 (From RVE NMD test)
	1064 – 3694 (From RVE NYM test)

## 7.5 Design Guide for SN Metamaterials

For Type 1 SN metamaterial, the wider bandgap in high frequency range is easier to produce by NYM than NMD. Therefore, a smaller mass or larger stiffness for the NYM resonator is used to broaden the bandgap region with high frequencies. On the other hand, for the NMD resonator, a large mass and large stiffness generally result in a broader bandgap, and the resonator's stiffness has even greater influence than the resonator's mass. However, since a low-frequency gap is desired for metamaterials, large resonator's mass is still recommended for the NMD model. As a result, the appropriate design is to use large mass and large stiffness for the NMD resonator to forbid low frequency waves, and apply small mass and large stiffness of the NYM resonator to block high frequency waves. By combining NMD and NYM bandgaps, a metamaterial for filtering waves with low frequencies in wider range is achieved.

For Type 2 SN metamaterial, a large mass and small stiffness of the NYM resonator is effective to shift the bandgap region to low frequencies. However, the bandwidth shrinks drastically with the increment of the mass of the resonator. As a result, for Type 2 SN metamaterial, a median mass of the NYM resonator is recommended.

For Type 3 SN metamaterial, although a large mass of two NYM resonators (frame stretching mode and internal masses symmetrical motion are the two NYM resonators) can reduce the lower bound of the bandgap, it also narrows the bandwidth. Therefore, a median mass of the NYM resonator is recommended. Trial and error of the stiffness of NYM resonators are required after specifying the mass of NYM resonator. Since the internal masses serve as NYM and NMD resonators, once the material properties of the NYM resonator is set, the NMD resonator is determined.



## 7.6 Summary

Three types of SN microstructures are designed for metamaterials in this study. Parametric studies are made to obtain the metamaterial with a broad bandgap in low frequency range. It is found that the frame stretching mode is more effective than using beam bending mode in designing broadband SN metamaterials. Moreover, by adding internal mass components, the bandgap can be significantly expanded.

In addition, an RVE steady-state analysis to determine bandgap regions is found to be quite accurate as compared with that based on dispersion curves.

The broadband metamaterials proposed in this study are fabricated using a 3D printer.

## 8. REFERENCES

- Ao, X., Chan, C.T., 2010. Negative group velocity from resonances in two-dimensional phononic crystals. *Wave Random Complex* 20, 276-288.
- Aydin, K., Guven K., 2005. Observation of negative refraction and negative phase velocity in left-handed metamaterials. *Appl. Phys. Lett.* 86, 124102.
- Boyd, R.W., Gauthier, D.J., 2002. Slow' and 'Fast' light. *Progress in Optics* 43, 497-530.
- Boyd, R.W., Gauthier, D.J., 2009. Controlling the velocity of light pulses. *Science* 326, 1074-1077.
- Brillouin, L., 1953. *Wave Propagation in Periodic Structures*, Dover, New York.
- Capolino, F., 2009. *Applications of Metamaterials*. CRC Press.
- Cui, T.J., Smith, D.R., Liu, R., 2010. *Metamaterials: Theory, Design, and Applications*, Springer.
- Chen, H., Fung, K.H., Ma, H., Chan, C.T., 2008. Polarization gaps and negative group velocity in chiral phononic crystals: Layer multiple scattering method. *Phys. Rev. B* 77, 224304.
- Cheng, Y., Xu, J.Y., Liu, X.J., 2008. One-dimensional structured ultrasonic metamaterials with simultaneously negative dynamic density and modulus. *Physical Review B* 77, 045134.
- Ding, Y., Liu, Z., Qiu, C., Shi, J., 2007. Metamaterial with simultaneously negative bulk modulus and mass density. *Physical Review Letter* 99, 093904.
- Drugan, W.J., 2007. Elastic composite materials having a negative stiffness phase can be stable. *Physical Review Letter* 98, 055502.
- Fang, N., Xi, D., Xu, J., Ambati, M., Srituravanich, W., Sun, C., Zhang, X., 2006. Ultrasonic metamaterials with negative modulus. *Nature Materials* 5, 452-456.
- Feigenbaum, E., Kaminski, N., Orenstein, M., 2009. Negative dispersion: a backward wave or fast light? *Nanoplasmonic examples*. *Optic Express* 17, 18934.
- Fok, L., Zhang, X., 2011. Negative acoustic index metamaterial. *Phys. Rev. B*, 83, 214304
- Hu, G.K., Huang, G.L., Sun, C.T., 2011. An elastic metamaterial with simultaneously negative mass density and bulk modulus, *Appl. Phys. Lett.* 98, 251907.
- Huang, H.H., Sun, C.T., 2009. Wave attenuation mechanism in an acoustic metamaterial with negative effective mass density. *New Journal of Physics* 11, 013003.

- Huang, H.H., Sun, C.T., Huang, G.L., 2009. On the negative effective mass density in acoustic metamaterials. *International Journal of Engineering Science* 47, 610-617.
- Huang, H.H., Sun, C.T., 2011a. Theoretical investigation of the behavior of an acoustic metamaterial with extreme Young's moduli. *J. Mech. Phys. Solids* 59, 2070-2081.
- Huang, H.H., Sun, C.T., 2011b. Locally resonant acoustic metamaterials with 2D anisotropic effective mass density. *Philos. Mag.* 91, 981-996.
- Islam, M.T., and Newaz, G., 2012. Metamaterial with mass-stem array in acoustic cavity. *Appl. Phys. Lett.* 100, 011904
- Jagliniski, T., Kochmann, D., Stone, D., Lakes, R.S., 2007. Composite materials with viscoelastic stiffness greater than diamond. *Science* 315, 620-622.
- Lakes, R.S., Lee, T., Bersie, A., Wang, Y.C., 2001. Extreme damping in composite materials with negative-stiffness inclusions. *Nature* 410, 565-567.
- Lakhtakia, A., McCall, M.W., Weighofer, W. S., 2002. Brief overview of recent developments on negative phase-velocity mediums (alias left-handed materials). *Int. J. Electron. Communications* 56, 407-410.
- Lamb, H., 1904. On group-velocity. *Proc. London Math. Soc.* 1, 473-479.
- Lindell, I.V., Tretyakov, S.A., Nikoskinen, K.I., Ilvonen, S., 2001. BW media – media with negative parameters, capable of supporting backward waves. *Microw. Opt. Technol. Lett.* 31, 129-133.
- Lee, S.H., Park, C.M., Seo, Y.M., Wang, Z.G., Kim, C.K., 2009a. Acoustic metamaterial with negative density. *Physics Letters A* 373, 4464-4469.
- Lee, S.H., Park, C.M., Seo, Y.M., Wang, Z.G., Kim, C.K., 2009b. Acoustic metamaterial with negative modulus. *Journal of Physics: Condensed Matter* 21, 175504.
- Lee, S.H., Park, C.M., Seo, Y.M., Wang, Z.G., Kim, C.K., 2010. Composite acoustic medium with simultaneously negative density and modulus. *Physical Review Letter* 104, 054301.
- Li, J., Chan, C.T., 2004. Double-negative acoustic metamaterial. *Physical Review E* 70, 055602.
- Li, J., Fok, L., Yin, X., Bartal, G., Zhang, X., 2009. Experimental demonstration of an acoustic magnifying hyperlens. *Nature Materials* 8, 931-934.
- Liu, Z., Chan, C.T., Sheng, P., 2005. Analytic model of phononic crystals with local resonances. *Physical Review B* 71, 014103.
- Liu, Z., Zhang, X., Mao, Y., Zhu, Y.Y., Yang, Z., Chan, C.T., Sheng, P., 2000. *Science*, 289, 1734 (2000).
- Meng, H., Wen, J., Zhao, H., Wen, X., 2012. Optimization of locally resonant acoustic metamaterials on underwater sound absorption characteristics. *Journal of Sound and Vibration* 331, 4406-4416.
- Milton, G.W., Willis, J.R., 2007. On modifications of Newton's second law and linear continuum elastodynamics. *Proceedings of the Royal Society A* 463, 855-880.
- Notomi, M., 2000. Theory of light propagation in strongly modulated photonic crystals: Refractionlike behavior in the vicinity of the photonic band gap. *Phys. Rev. B* 62, 10696.
- Schuster, J. A., 1904. *An Introduction to the Theory of Optics*. Edward Arnold, London
- Shelby, R.A., Smith, D.R., Schultz, S., 2001. Experimental verification of a negative index of refraction. *Science* 292, 77-79.

- Smith, D.R., Padilla, W.J., Vier, D.C., Nemat-Nasser, S.C., Schultz, S., 2000. Composite medium with simultaneously negative permeability and permittivity. *Physical Review Letter* 84, 4184-4187.
- Pendry, J.B., 2000. Negative refraction makes a perfect lens. *Physical Review Letter* 85, 3966-3969.
- Veselago, V.G., 1968. The electrodynamics of substances with simultaneously negative values of  $\epsilon$  and  $\mu$ . *Soviet Physics Uspekhi* 10, 509-514.
- Wang, L. J., Kuzmich, A., Dogariu, A., 2000. Gain-assisted superluminal light propagation. *Nature* 406, 277-279.
- Yao, S., Zhou, X., Hu, G., 2008. Experimental study on negative mass effective mass in a 1D mass-spring system. *New Journal of Physics* 10, 043020.
- Zigoneanu, L., Popa, B.I., Starr, A.F., Cummer, S.A., 2011. Design and measurements of a broadband two-dimensional acoustic metamaterial with anisotropic effective mass density. *Journal of Applied Physics* 109, 054906.

## 9. PUBLICATIONS

- H. H. Huang and C. T. Sun, "Locally Resonant Acoustic Metamaterials with 2D Anisotropic Effective Mass Density," *Philosophical Magazine*, Vol. 91, No.6, 2011, pp. 981-996.
- R. Zhu, H.H. Huang, G. L. Huang, and C. T. Sun, "Microstructure Continuum Modeling of an Elastic Metamaterial," *Int. J. Engineering Science*, Vol. 49, 2011, pp. 1477-1485.
- H. H. Huang and C. T. Sun, "A study of Band-gap Phenomena of Two Locally Resonant Acoustic Metamaterials," *J. Nanoengineering and Nanosystems*, Nov. 25, 2011, pp. 83-91.
- X. N. Liu, G. K. Hu, C.T. Sun, and G. L. Huang, "Wave Propagation Characterization and Design of Two-Dimensional Elastic Chiral Metacomposite," *J. of Sound and Vibration*, 330, pp. 2536-2553, 2011
- X.N. Liu, G. K. Hu, G. L. Huang, and C.T. Sun, "An Elastic Metamaterial with Simultaneously Negative Mass Density and Bulk Modulus," *Applied Physics Letters*, 98, 251907, 2011.
- H.H. Huang and C.T. Sun, "Theoretical Investigation of the Behavior of an Acoustic Metamaterial with Extreme Young's Modulus," *J. Mechanics and Physics Solids*, doi:10.1016/j.jmps.2011.07.002, 2011.
- R. Zhu, G. L. Huang, H.H. Huang, and C. T. Sun, "Experimental and Numerical Study of Guided Wave Propagation in a Thin Metamaterial Plate," *Physics Letters A*, 375, , 2011, pp. 2863-2867
- H.H. Huang and C.T. Sun, "Continuum Modeling of a Composite Material with Internal Resonators," *Mechanics of Materials*, 46, 2012, pp.1-10.
- H.H. Huang and C.T. Sun, "Anomalous Wave Propagation in a One-dimensional Acoustic Metamaterial Having Simultaneously Negative Mass Density and Young's Modulus," *Journal of Acoustical Society of America*, 132(4), October 2012, pp.2887-95

- R. Zhu, X. N. Liu, Guoliang Huang, Hsin-Haou Huang, and C.T. Sun, “Microstructure Design and Experimental Validation of Elastic Metamaterial Plates with Anisotropic Mass Density,” *Physical Review B*, Vol. 86, No. 14, October 2012, 144307.
- K.T. Tan, H.H. Huang and C.T. Sun, “Optimizing the Band Gap of Effective Mass Negativity in Acoustic Metamaterials,” *Applied Physics Letters*, 101: 241902, 2012.
- Kota Mikoshiba, James M. Manimala and C.T. Sun, “Energy Harvesting Using an Array of Multifunctional Resonators,” *Journal of Intelligent Material Systems and Structures*, Vol 24, January 2013, pp. 168 - 179.
- R. Zhu, X. N. Liu, G. K. Hu, , C.T. Sun, and G. L. Huang, “A Chiral Elastic Metamaterial Beam for Broadband Vibration Suppression,” *J. of Sound and Vibration*, 333, 2014, pp. 2759-2773.
- K.T. Tan, H.H. Huang and C.T. Sun, “Blast-Wave Impact Mitigation Using Negative Effective Mass Density Concept of Elastic Metamaterials,” *International Journal of Impact Engineering*, Engineering, Vol. 64, 2014, pp. 20-29.
- James M. Manimala and C. T. Sun, “Microstructural Design Studies for Locally Dissipative Acoustic Metamaterials,” *J Applied Physics*, 115, 023518 (2014).
- James M. Manimala, Hsin Haou Huang, C. T. Sun, Robert Snyder and Scott Bland, “Dynamic Load Mitigation using Negative Effective Mass Structures,” *Engineering Structures*, Volume 80, December 2014, Pp. 458–468.
- Y. Chen, G.L. Huang, X.M. Zhou, G.K. Hu, and C.T. Sun, “Analytical coupled vibroacoustic modeling of membrane-type acoustic metamaterials: Membrane model,” *Journal of the Acoustical Society of American*, Vol. 136, No.3, September 2014.
- Yongquan Liu, Xianyue Su, C.T. Sun, “Broadband Elastic Metamaterial with Single Negativity by Mimicking Lattice Systems,” *J of the Mechanics and Physics of Solids*, to appear.
- R. Zhu, X. N. Liu, G. K. Hu, C. T. Sun and G. L. Huang, “Negative Refraction of Elastic Waves at the Deep Subwavelength Scale in a Single-Phase Metamaterial,” *Nature Communication*, 2014, accepted.
- Y. Chen, G.L. Huang, and C.T. Sun, “Band Gap Control in an Active Elastic Metamaterial with Negative Capacitance Piezoelectric Shunting,” *ASME Journal of Vibration and Acoustics*, in press.